foundations

MDPI

Article

Harmonic-Assisted Parametric Excitation in Coupled Resonant Systems: Theory and Experimental Validation

Esa Ruoho [1,*], Jukka Kortela [2] and Michael Gasik [2]

[1] Independent Researcher, FI-00990 Helsinki, Finland
[2] School of Chemical Engineering, Aalto University, P.O. Box 16100, FI-00076 Aalto, Finland; jukka.kortela@aalto.fi (J.K.); michael.gasik@aalto.fi (M.G.)
* Correspondence: esaruoho@gmail.com

Abstract

The classical mass–spring–damper and inductor–capacitor–resistor analogy is extended from constant to state-dependent parameters and connected to an experimentally realized coupled Metglas AMCC-1000 resonant magnetic system. The formulation distinguishes externally varying inductance from intrinsic magnetic nonlinearity through secant and differential inductance and incorporates reversible, dissipative, and externally driven dynamics. The experimental study combines coupled-mode design with synchronized voltage and RF-current measurements. Measured component values establish a 32.016/16.461 kHz resonant pair with a frequency ratio of 1.9449, while calibrated RF-probe analysis quantifies the corresponding current components and broadband measurements reveal higher harmonic structure. A complementary 11–13 kHz controlled frequency sweep was performed at fixed 22 V, 388 mA supply conditions and 18% duty cycle. Coherent least-squares analysis identifies a common maximum of the second-order component at an 11.5 kHz drive frequency in two voltage channels and the RF-current channel, with $A(2f_d)/A(f_d)$ ratios of 0.809, 0.870, and 3.665, respectively. The associated trigger-origin-invariant harmonic phase relation provides complementary phase-domain evidence of an organized frequency-selective nonlinear response. The results establish a reproducible connection between state-dependent oscillator theory, coupled-resonator design, and experimentally measurable harmonic dynamics.

Keywords: mechanical–electrical analogy; parametric excitation; fractional-order operator; negative resistance; aeroelastic flutter; parametric anti-resonance

Check for updates

Academic Editors: António Lopes and Luigi Rodino

Received: 31 July 2026
Revised: 5 September 2026
Accepted: 29 September 2026
Published: 1 October 2026

Copyright: © 2026 by the authors. Licensee MDPI, Basel, Switzerland. This article is an open access article distributed under the terms and conditions of the Creative Commons Attribution (CC BY) license.

1. Introduction

The analogy between mechanical and electrical oscillators has been one of the cornerstones of engineering science for more than a century. The correspondence between inertia and inductance, viscous damping and electrical resistance, and elastic stiffness and capacitance provides a common mathematical framework for describing oscillatory phenomena across multiple physical domains [1]. Because both systems satisfy second-order differential equations, this analogy has become fundamental in physics, electrical engineering, mechanics, control theory, and system modelling.

In nearly all classical treatments, however, the analogy is restricted to constant system parameters. Real engineering systems rarely satisfy this assumption. Mechanical inertia, stiffness, damping, magnetic permeability, inductance, resistance, and capacitance may all vary with displacement, current, magnetic field, mechanical loading, temperature, or time.

Once these state-dependent parameters are admitted, additional coupling terms naturally emerge in both domains. These parametric terms are not mathematical curiosities but represent physically measurable energy-transfer mechanisms that enable phenomena such as parametric amplification, oscillation, instability, and energy conversion.

Recent developments in fractional-order modelling, state-dependent dynamics, and metriplectic formulations have further demonstrated that the classical oscillator analogy is considerably more general than traditionally assumed. The reversible energy-storage mechanisms and irreversible dissipation processes remain structurally identical even when the system coefficients become dynamic.

This broader interpretation provides a common structural language for passive variable-coefficient systems, while active elements, negative resistance, and externally driven parametric excitation are represented explicitly as open-system energy-injection or modulation mechanisms coupled to the passive oscillator.

Although the theoretical foundations of parametric excitation are well established, comparatively few studies have progressed from mathematical models to experimentally realizable high-power magnetic structures operating under practical design constraints. In particular, the design of a physically realizable parametric transformer requires simultaneous optimization of magnetic geometry, resonant tuning, coupled inductances, winding topology, quality factors, mutual coupling, capacitor tolerances, and nonlinear magnetic behaviour. Achieving the required frequency relationship while maintaining stable resonance under realistic loading conditions represents a considerably more demanding engineering problem than the idealized Mathieu-equation models commonly presented in the literature.

The present work addresses this gap by combining the generalized state-dependent oscillator formulation with the practical design methodology of a Metglas AMCC-1000-based parametric transformer operating at its resonant operating point [2]. Rather than considering only idealized differential equations, the work develops a complete engineering design procedure including magnetic-gap estimation, inductance extraction, coupled-mode analysis, resonant optimization, tolerance analysis, Monte Carlo verification, and an experimentally executable tuning protocol. Particular emphasis is placed on establishing the required 2:1 frequency relationship between the pump and output resonators while accounting for mutual coupling, finite quality factors, nonlinear magnetic behaviour, and practical component tolerances.

The principal novelty of this work is therefore not the existence of parametric resonance itself, but the presentation of a complete engineering methodology for designing, tuning, and experimentally validating a practical AMCC-1000 parametric transformer operating under resonant conditions. The proposed procedure connects the theoretical framework of state-dependent oscillators directly with experimentally measurable electrical and magnetic quantities, thereby providing a reproducible path from mathematical theory to laboratory implementation.

This paper is organized as follows. Section 2 revisits the classical mechanical–electrical analogy and identifies its implicit constant-parameter assumption. Section 3 derives the generalized state-dependent formulation and establishes the corresponding mechanical and electrical parametric terms. Section 4 interprets inductive, resistive, and capacitive elements as integer-order members of a unified fractional-order operator family. Section 5 extends the analogy to active systems, negative resistance, and aeroelastic flutter. Section 6 discusses parametric excitation, energy transfer, and the associated Manley–Rowe constraints. Section 7 presents the metriplectic interpretation that unifies the reversible and dissipative dynamics. Sections 8–10 develop the practical design methodology for a resonant AMCC-1000 parametric transformer, including resonance optimization, coupled-mode analysis, tolerance simulations, and experimental tuning procedures. Section 11 presents the initial

experimental validation, including simultaneous voltage- and RF-current-probe measurements, direct characterization of the approximately 32 kHz/16 kHz resonant operating pair, calibrated RF-current estimates, and broadband FFT and harmonic-overtone analysis from 1 kHz to 1 MHz. Section 12 presents the controlled 11–13 kHz frequency-sweep validation performed under fixed 22 V, 388 mA supply conditions and an 18% duty cycle. This section introduces coherent least-squares analysis of the fundamental and second-order components and the trigger-origin-invariant harmonic phase quantity $\Psi_{21} = 2\phi_1 - \phi_2$, and demonstrates a common frequency-localized enhancement of the $2f_d$ response at a drive frequency of 11.5 kHz across both voltage channels and the RF-current-probe channel. Finally, Section 13 summarizes the principal theoretical, engineering, and experimental conclusions and identifies the remaining measurements required for complete quantitative characterization of parametric energy transfer.

2. The Classical Analogy and Its Implicit Assumption

The classical analogy between mechanical and electrical oscillators is based on the observation that both systems are governed by mathematically identical second-order differential equations. A single-degree-of-freedom mechanical oscillator with mass m, viscous damping c, stiffness k, and external force $F(t)$ satisfies

$$m\,\ddot{x} + c\,\dot{x} + k\,x = F(t). \tag{1}$$

Similarly, a series RLC circuit with inductance L, resistance R, capacitance C, and excitation voltage $V(t)$, expressed in terms of charge q ($I = \dot{q}$), is described by

$$L\,\ddot{q} + R\,\dot{q} + \frac{1}{C}q = V(t). \tag{2}$$

The structural equivalence of Equations (1) and (2) forms the basis of the classical impedance analogy, in which force corresponds to voltage and mass to inductance [1]. The complete correspondence between the mechanical and electrical variables is summarized in Table 1. Under the same mapping, the stored kinetic and elastic energies are directly associated with magnetic and electric field energies,

$$\underbrace{\frac{1}{2}m\dot{x}^2}_{\text{kinetic}} \leftrightarrow \underbrace{\frac{1}{2}LI^2}_{\text{magnetic}}, \qquad \underbrace{\frac{1}{2}kx^2}_{\text{elastic}} \leftrightarrow \underbrace{\frac{1}{2C}q^2}_{\text{electric}}. \tag{3}$$

Table 1. Classical impedance analogy between mechanical and electrical oscillators.

Mechanical	↔	Electrical
Displacement x		Charge q
Velocity $\dot{x}$		Current $I = \dot{q}$
Force F		Voltage V
Mass m		Inductance L
Damping c		Resistance R
Stiffness k		Inverse capacitance $1/C$

An alternative representation is provided by Firestone's mobility analogy, which interchanges the across and through variables by identifying force with current and velocity with voltage [3]. Although the two analogies differ in variable assignment, they preserve the same second-order mathematical structure. As emphasized by Olson [1], the correspondence is therefore formal rather than physical: the lumped mechanical and electrical elements represent the coefficients of identical governing differential equations. Throughout this work, the impedance analogy is adopted.

An important invariant under both analogies is the quality factor,

$$Q = \frac{\omega L}{R}$$

for electrical oscillators and

$$Q = \frac{\omega m}{c}$$

for mechanical oscillators. In both cases, Q measures the ratio of stored energy to energy dissipated per radian and therefore determines the resonance bandwidth according to $\Delta\omega = \omega_0/Q$ [4]. The frequency-domain representation employed later in Section 5 is based on Steinmetz's symbolic method [5], in which sinusoidal differential equations are transformed into algebraic equations through the complex operator $j\omega$. This formulation provides the common mathematical foundation for impedance analysis in both electrical and mechanical systems.

The classical analogy implicitly assumes that all system parameters,

$$m,\ c,\ k,\ L,\ R,\ \text{and}\ C,$$

remain constant. Consequently, Equations (1)–(3) describe only linear time-invariant systems. This assumption is rarely stated explicitly in the classical literature, yet it underlies virtually all textbook treatments of the analogy. The central objective of the present work is to remove this restriction and investigate whether the structural correspondence remains valid when the governing parameters become state-dependent or time-varying. As will be shown in the following sections, allowing variable coefficients naturally introduces parametric coupling terms while preserving the fundamental mathematical equivalence between the mechanical and electrical domains.

3. Releasing the Constant-Parameter Assumption: Electromagnetic Systems

The classical oscillator analogy presented in Section 2 assumes that the electrical parameters remain constant. In practical electromagnetic devices, however, this assumption is generally not valid. In particular, a nonlinear magnetic core is more fundamentally described by its flux linkage

$$\lambda = \lambda(I, \theta, T, t), \tag{4}$$

where I denotes the winding current, θ represents the mechanical or magnetic configuration (including, for example, the effective air gap), T is temperature, and t allows explicit external modulation.

For a nonlinear magnetic characteristic, two inductances must be distinguished. The secant inductanceis defined by

$$L_{\text{sec}} = \frac{\lambda(I, \theta, T, t)}{I}, \qquad I \neq 0, \tag{5}$$

whereas the *differential* or *incremental inductance* is

$$L_{\text{diff}} = \left.\frac{\partial \lambda}{\partial I}\right|_{\theta, T, t}. \tag{6}$$

These quantities are identical only in the linear magnetic limit. Throughout the nonlinear dynamical formulation below, the coefficient multiplying dI/dt is the differential inductance L_{diff}. The secant inductance is used only when the flux linkage is represented algebraically as $\lambda = L_{\text{sec}} I$ or when an effective small-signal or measured resonant inductance is explicitly reported.

The inductor voltage follows from Faraday's law as

$$V_L = \frac{d\lambda}{dt}. \tag{7}$$

Applying the chain rule to Equation (4) gives

$$V_L = \frac{\partial \lambda}{\partial I}\frac{dI}{dt} + \frac{\partial \lambda}{\partial \theta}\frac{d\theta}{dt} + \frac{\partial \lambda}{\partial T}\frac{dT}{dt} + \left.\frac{\partial \lambda}{\partial t}\right|_{I,\theta,T}. \tag{8}$$

Accordingly,

$$V_L = L_{\text{diff}}\frac{dI}{dt} + V_{\text{par}}, \tag{9}$$

where

$$V_{\text{par}} = \frac{\partial \lambda}{\partial \theta}\dot{\theta} + \frac{\partial \lambda}{\partial T}\dot{T} + \left.\frac{\partial \lambda}{\partial t}\right|_{I,\theta,T} \tag{10}$$

collects the voltage contributions produced by changes of parameters other than the instantaneous current itself.

In the important special case in which the magnetic element can be represented by a current-independent but externally time-varying inductance,

$$\lambda = L(t)I, \tag{11}$$

Equation (8) reduces to

$$V_L = L\frac{dI}{dt} + I\frac{dL}{dt}. \tag{12}$$

Thus, the familiar term $I(dL/dt)$ is retained as the parametric-voltage term for externally modulated inductance, but it should not be interpreted as the general nonlinear-core correction when L itself depends on I. For a nonlinear magnetic core, the current-dependent contribution is already contained in $L_{\text{diff}} = \partial\lambda/\partial I$.

Externally driven variations of the magnetic parameters provide a mechanism through which energy can be exchanged between the modulation source and the electrical resonator. The flux-linkage formulation above makes this distinction explicit while preserving the correspondence with the variable-coefficient mechanical system developed in the following section.

An entirely analogous result is obtained for a variable capacitor. If the capacitance depends on voltage, geometry, dielectric properties, temperature, or time,

$$I_C = \frac{d}{dt}(CV) = C\frac{dV}{dt} + V\frac{dC}{dt}, \tag{13}$$

where the second term,

$$V\frac{dC}{dt},$$

is the capacitive counterpart of the inductive parametric voltage. Consequently, relaxing the assumption of constant electrical parameters introduces exactly one additional coupling term for each reactive element. These parametric terms constitute the fundamental extension of the classical oscillator equations and provide the mathematical basis for parametric amplification, frequency conversion, and resonant energy transfer considered in the following sections.

4. Releasing the Constant-Parameter Assumption: Mechanical Systems

Relaxing the constant-parameter assumption is equally natural on the mechanical side. At this point, however, it is important to distinguish between two physically different situations: a time-dependent effective inertia and a body whose physical mass changes through exchange of matter with its surroundings. In the former case, the coefficient multiplying the acceleration may vary because of geometry, configuration, constraints, attached or redistributed inertia, or externally controlled inertial properties, without any

mass crossing the system boundary. In the latter case, the system is an open variable-mass system and the momentum flux associated with the exchanged matter must be included explicitly. The Meshchersky equation applies specifically to this second case. Both situations can produce variable inertial coefficients in an oscillator model, but they must not be identified physically.

4.1. Variable Effective Inertia and Open Variable-Mass Systems

We first consider the more general oscillator description in terms of a time-dependent effective inertial coefficient $m_{\text{eff}}(t)$. This notation does not imply that physical mass enters or leaves the mechanical system. Defining the generalized momentum associated with this effective inertia as

$$p = m_{\text{eff}}(t)\dot{x},$$

and Newton's second law follows from the time derivative of the momentum,

$$\frac{d}{dt}(m_{\text{eff}}\dot{x}) = m_{\text{eff}}\ddot{x} + \dot{m}_{\text{eff}}\dot{x}. \tag{14}$$

The additional contribution,

$$\dot{m}_{\text{eff}}\dot{x},$$

appears because the effective inertial coefficient is time-dependent. It is a product-rule term and, by itself, does not imply physical mass exchange. Under the impedance analogy introduced in Section 2, its mathematical counterpart is the electrical term

$$I\frac{dL}{dt},$$

obtained in Equation (8) for an externally time-varying inductance. The correspondence established here is therefore between variable effective inertia and variable inductive energy storage at the level of the oscillator equations. It should not be interpreted as asserting that every time-dependent inertial coefficient represents a Meshchersky variable-mass system.

A physically distinct special case arises when $m(t)$ denotes the actual mass of a body and changes because matter enters or leaves the system. Such a system is an open mechanical system, and the variation of $m(t)$ cannot in general be represented solely by replacing a constant inertial coefficient with a prescribed function of time. The exchanged matter carries momentum, and the associated momentum flux must be included explicitly. For this physical mass-exchange problem, the equation of motion is the Meshchersky equation [6,7],

$$m\ddot{x} = F_{\text{ext}} + \frac{dm}{dt}u_{\text{rel}}, \tag{15}$$

where

$$u_{\text{rel}} = u - \dot{x}$$

is the velocity of the incoming or outgoing mass relative to the body.

The term

$$\frac{dm}{dt}u_{\text{rel}}$$

is the momentum-flux contribution associated specifically with physical mass exchange and is commonly referred to as the Meshchersky force. It has no necessary counterpart in a closed mechanical system whose effective inertia varies without mass crossing the system boundary. The simplified momentum equation

$$\frac{d}{dt}(m\dot{x}) = F_{\text{ext}}$$

therefore cannot be used as a general equation for an open variable-mass body; its validity depends on the definition of the system and on the velocity of the exchanged mass. This distinction has been discussed extensively in the variable-mass literature because omission or misinterpretation of the momentum-flux contribution has historically led to misconceptions in classical mechanics texts [8–10].

In the present work, the Meshchersky equation is included as an important open-system extension, but it is not taken as the general definition of variable inertia. The primary mechanical analogue used in the oscillator correspondence is the time-dependent effective inertial coefficient $m_{\text{eff}}(t)$. Meshchersky dynamics represents the more specific case in which the changing inertial mass results from actual mass exchange and an additional momentum port is therefore present. In this open-system case, the Meshchersky momentum-flux term provides a mechanical example of exchange with the surroundings, conceptually analogous to treating externally driven electromagnetic parameter modulation through an explicit external energy port.

The continuum formulation leads to the same conclusion. Applying the linear momentum theorem to an open control volume yields the reactive momentum-flux term

$$-\int_{\partial D(t)} \mathbf{v}(\mathbf{v}-\mathbf{w})\cdot\mathbf{n}\,\rho\,dS,$$

which vanishes only when the control surface moves with the material ($\mathbf{w}=\mathbf{v}$) and becomes non-zero whenever mass crosses the system boundary [11].

This continuum result reinforces the distinction made above: systems involving actual mass transport across their boundaries are open systems and require momentum-flux terms, whereas a prescribed time-dependent effective inertia in a closed oscillator need not involve any mass flux. The two cases may share related variable-coefficient mathematical structures, but their physical interpretations and conservation-law closures are different.

The structural equivalence between the electrical and mechanical formulations becomes evident by comparing the product-rule expansions of flux linkage,

$$\lambda = LI,$$

and momentum,

$$p = m\dot{x}.$$

Differentiation yields

$$V = \frac{d\lambda}{dt} = L\frac{dI}{dt} + I\frac{dL}{dt}, \qquad F = \frac{dp}{dt} = m\ddot{x} + \dot{x}\frac{dm}{dt}. \tag{16}$$

Using the impedance correspondence

$$L \leftrightarrow m, \qquad I \leftrightarrow \dot{x}, \qquad V \leftrightarrow F,$$

introduced in Section 2, both expressions become identical term by term. The constant-coefficient terms correspond directly to the classical oscillator equations, whereas the additional terms satisfy the structural identity

$$\boxed{I\frac{dL}{dt} \;\longleftrightarrow\; \dot{x}\frac{dm}{dt}}. \tag{17}$$

Equation (17) therefore follows unavoidably from the product rule whenever either inertial coefficient is allowed to vary. The cross term disappears only in the limiting case where both L and m remain constant.

4.2. Variable Elasticity and Complex Stiffness

State-dependent mechanical parameters are not limited to inertia. Structural dynamics has long incorporated variable elastic behaviour through the concept of complex stiffness,

$$k \to k(1 + ig), \tag{18}$$

where g denotes the dimensionless hysteretic damping coefficient [12]. In this representation, energy dissipation is associated directly with the elastic element rather than with a separate viscous damper.

As noted by Neumark [12], the resulting force–displacement relationship forms a closed hysteresis loop that closely resembles the magnetic B–H hysteresis characteristic of ferromagnetic materials. The parameter g therefore represents the mechanical loss angle in the same sense that magnetic hysteresis represents energy dissipation in nonlinear magnetic cores. Consequently, hysteretic elasticity extends the classical energy correspondence of Equation (3) by allowing irreversible energy dissipation to be associated directly with the elastic coordinate, thereby providing a natural mechanical counterpart to magnetic core losses discussed in Section 3.

5. A Unified Fractional-Order Representation

The classical oscillator elements differ only in the frequency dependence of their impedance. In the frequency domain,

$$Z_L = L(j\omega), \qquad Z_R = R, \qquad Z_C = \frac{1}{C}(j\omega)^{-1}, \tag{19}$$

with the corresponding mechanical elements following the same scaling under the impedance analogy: inertance is proportional to $(j\omega)^{+1}$, viscous damping to $(j\omega)^{0}$, and elastic compliance to $(j\omega)^{-1}$. Consequently, all three elements can be regarded as integer-order realizations of the generalized fractional-order constitutive relation [13–15]

$$y = kD^{\alpha}x, \qquad \alpha \in \{+1, 0, -1\}, \tag{20}$$

where D^{α} denotes a fractional derivative in the Riemann–Liouville or Caputo sense. The cases $\alpha = +1$, 0, and -1 recover the inductive (inertial), resistive (damping), and capacitive (elastic) elements, respectively. Throughout this work, the mechanical coefficient k denotes stiffness, yielding the correspondence

$$k \leftrightarrow \frac{1}{C},$$

as summarized in Table 1. The equivalent compliance representation, $1/k \leftrightarrow C$, is mathematically identical but is not used here.

The significance of Equation (20) extends beyond the integer-order cases. Physical systems frequently exhibit fractional-order behaviour characterized by the generalized impedance

$$Z = K(j\omega)^{\alpha}, \qquad 0 < |\alpha| < 1,$$

which describes electrical fractance or constant-phase elements arising in distributed RC networks and electrode–electrolyte interfaces [13].

An analogous situation exists in mechanics. Bagley and Torvik [16] demonstrated that the constitutive behaviour of linear viscoelastic materials is governed by a fractional-order stress–strain relation,

$$\sigma(t) = E_0\varepsilon(t) + E_1D^{\beta}\varepsilon(t), \qquad 0 < \beta < 1, \tag{21}$$

resulting in a dynamic modulus proportional to $(j\omega)^{\beta}$. Importantly, the fractional exponent follows directly from molecular theory rather than empirical curve fitting. For the Rouse polymer model, $\beta = 1/2$, whereas Zimm's model predicts $\beta = 2/3$ [16]. Fractional-order constitutive behaviour therefore arises naturally from the underlying material microstructure.

These results extend the earlier observations of Gemant and Scott-Blair, who recognized that the dynamic stiffness and damping of viscoelastic materials follow fractional powers of frequency. Their work established the foundations of modern fractional viscoelasticity later formalized by Caputo and subsequently developed by Bagley and Torvik. Equation (21) is therefore the mechanical counterpart of the electrical fractance element represented by Equation (20).

Koeller [17] introduced the corresponding mechanical element explicitly as the *spring-pot*,

$$\sigma = ED^{\beta}\varepsilon,$$

which continuously interpolates between a Hookean spring ($\beta = 0$) and a Newtonian dashpot ($\beta = 1$). Its creep and relaxation responses are governed by the Mittag–Leffler function, while experimentally observed values typically satisfy $0.05 \lesssim \beta \lesssim 0.35$. The spring-pot is therefore the direct mechanical analogue of the electrical constant-phase element: both represent fractional-order realizations of Equation (20). Consequently, the interval between the integer-order limits is populated by physically realizable elements in both electrical and mechanical systems.

Equation (20) therefore provides a unified interpretation of mechanical and electromagnetic oscillators. Rather than representing two merely analogous systems, both are manifestations of the same fractional-order dynamical structure, with the classical second-order oscillator corresponding to the limiting integer-order cases.

Domain-Independent Interpretation: The Metriplectic Formulation

The structural equivalence established in Sections 2–5 admits a coordinate-independent formulation using metriplectic dynamics. The state vector z evolves according to

$$\dot{z} = \mathcal{L}\,\delta E + \mathcal{M}\,\delta S, \tag{22}$$

where the antisymmetric Poisson operator $\mathcal{L}$ generates reversible energy-conserving dynamics and the symmetric metric operator $\mathcal{M}$ describes irreversible entropy production [18,19]. These operators satisfy the degeneracy conditions

$$\mathcal{L}\delta S = 0, \qquad \mathcal{M}\delta E = 0,$$

ensuring independent conservation of total energy and monotonic entropy production.

For a passive oscillator, $\mathcal{L}$ governs the reversible exchange between the two energy-storage mechanisms—kinetic and elastic energy in mechanics, magnetic and electric energy in electromagnetics (Equation (3))—whereas $\mathcal{M}$ represents the dissipative contribution associated with viscous damping or electrical resistance.

Within this framework, the impedance analogy of Section 2 expresses the fact that passive mechanical and electrical oscillators can be represented by corresponding reversible and dissipative structures, differing primarily in the physical interpretation of their state variables. State-dependent passive coefficients may be incorporated while retaining this decomposition, provided that the metric contribution continues to satisfy the positivity and degeneracy requirements of the metriplectic formulation.

An important qualification is required for active elements. In the standard metriplectic construction, the metric operator $\mathcal{M}$ is chosen so that the irreversible contribution has a definite sign and the associated entropy production is non-negative, together with the

degeneracy condition $\mathcal{M}\delta E = 0$. A negative electrical resistance or negative mechanical damping injects energy into the oscillator and therefore cannot, in general, be represented merely by reversing the sign of a standard positive-semidefinite metric operator while retaining all standard metriplectic properties. Such a sign reversal would make the dissipative operator indefinite or negative in the active subspace and would invalidate the usual monotonic-entropy interpretation.

Accordingly, in this work the term *metriplectic* is used strictly for the passive reversible–dissipative structure satisfying the conventional degeneracy and sign conditions. Negative resistance and aeroelastic negative damping are instead treated as externally powered or open-system contributions appended to the passive metriplectic dynamics. A convenient extended representation is

$$\dot{z} = \mathcal{L}\,\delta E + \mathcal{M}\,\delta S + \mathcal{F}_{\text{act}}(z,t), \tag{23}$$

where $\mathcal{F}_{\text{act}}$ represents active energy injection from an electrical supply, fluid flow, or another external reservoir. The passive part retains the standard metriplectic properties, whereas the complete open system is not required to exhibit monotonic entropy production with respect to the reduced oscillator variables alone.

Parametric pumping is likewise most precisely interpreted as explicit time dependence of the energy-storage structure or Hamiltonian parameters, with the modulation source providing an external power port. This distinction separates passive dissipation, active negative damping, and parametric energy exchange and avoids attributing all three mechanisms to the same metric operator.

6. Phenomena Beyond the Classical Constant-Coefficient Analogy

The classical oscillator analogy describes passive linear systems with constant parameters. Once active elements or state-dependent coefficients are introduced, additional dynamical phenomena emerge that cannot be represented within the classical formulation. Three particularly important examples are negative damping, parametric excitation, and nonlinear self-excited oscillation.

6.1. Negative-Loss Elements and Their Mechanical Counterparts

6.1.1. Negative Resistance and Self-Excited Oscillation

A negative real part of the electrical impedance transforms a damped oscillator into a self-excited system. The mechanical counterpart is aeroelastic flutter, in which aerodynamic forces inject energy into the structure rather than dissipating it.

The classical theory was established by Theodorsen [20], who showed that self-excited oscillation requires the coupling of at least two structural degrees of freedom. While a single vibration mode is always aerodynamically damped, coupled bending–torsion or wing–control-surface modes may extract energy from the surrounding airflow, producing exponentially growing oscillations above a critical flutter velocity. The aerodynamic forces act together with the inertial and elastic forces, thereby introducing an active energy-transfer mechanism absent from passive oscillators.

The same interpretation forms the basis of the classical flutter treatment by Bisplinghoff et al. [21] (Section 9), where bending–torsion coupling produces an instability once the effective damping becomes zero and subsequently negative.

6.1.2. Flutter as a Frequency-Dependent Complex Coefficient

The underlying mechanism of flutter is a frequency-dependent complex coefficient rather than a constant damping term. In Theodorsen's formulation, the unsteady aerodynamic forces are governed by the complex circulation function

$$C(k) = F(k) + iG(k),$$

where the reduced frequency is defined as

$$k = \frac{\omega b}{U}.$$

The imaginary component determines the phase relationship between the aerodynamic force and structural motion and therefore controls the net energy transfer during each oscillation cycle. Flutter occurs when the aerodynamic work changes sign and the airflow supplies energy to the structure rather than removing it [21] (Section 9.1).

In contrast, the quasi-steady approximation neglects this frequency dependence and predicts only positive aerodynamic damping. The instability therefore originates from the dynamic complex coefficient itself rather than from the static aerodynamic forces. This observation closely parallels the fractional-order constitutive behaviour discussed in Section 5, where the frequency-dependent operator introduces dynamics that cannot be represented by integer-order elements alone.

Neumark [12] reached the same conclusion by identifying the critical flight velocity at which the effective damping becomes zero. Above this threshold, the damping becomes negative and the oscillation amplitude increases exponentially. Aeroelastic flutter may therefore be interpreted as the mechanical analogue of electrical negative resistance.

6.1.3. The Van Der Pol Oscillator

The common mathematical description of self-excited oscillation is provided by the van der Pol equation,

$$\ddot{x} - \mu(1 - x^2)\dot{x} + x = 0,$$

whose nonlinear damping is negative for small amplitudes and positive for large amplitudes. Consequently, oscillations neither decay nor diverge but converge to a stable limit cycle.

Originally derived from the negative-resistance behaviour of triode circuits, with practical electronic realizations described by Page [22], the same equation was subsequently recognized by van der Pol as governing biological and mechanical oscillators, including the heartbeat [23]. Negative-resistance oscillators, aeroelastic flutter, and many forms of flow-induced instability therefore represent different physical realizations of the same nonlinear dynamical system.

6.1.4. Galloping and Flow-Induced Negative Damping

The general criterion for mechanically self-excited oscillation was formulated by Den Hartog [24] (Section 7): the oscillatory force must be generated by the motion itself so that the energy input disappears when the motion ceases. This condition is equivalent to negative effective damping.

A classic example is the galloping of ice-covered transmission lines [25]. Ice accumulation modifies the conductor cross-section, producing aerodynamic lift in addition to drag. The resulting variation of the angle of attack causes the aerodynamic force to acquire a component in the direction of motion, leading to large-amplitude, low-frequency oscillations.

The corresponding instability criterion is

$$\frac{dC_L}{d\alpha} + C_D < 0, \tag{24}$$

which directly identifies the onset of negative aerodynamic damping from static lift and drag characteristics. Nikitas and Macdonald [26] subsequently generalized this criterion to arbitrary angles of attack and coupled structural motion.

Galloping and flutter therefore represent different manifestations of the same physical mechanism. A closely related phenomenon is vortex-induced vibration, where synchronization between vortex shedding and structural motion produces lock-in. Wind-tunnel experiments further demonstrate that, when vortex shedding is suppressed, purely motion-induced oscillations can still be sustained through an effective negative damping mechanism generated by the structural motion itself [27].

The correspondence between the electrical and mechanical descriptions may therefore be written as

$$R < 0 \quad \Longleftrightarrow \quad c_{\text{eff}} < 0, \tag{25}$$

where negative electrical resistance corresponds directly to negative effective mechanical damping.

6.1.5. Coupled Electrical and Mechanical Negative Damping

An important engineering example in which both mechanisms coexist is subsynchronous resonance in turbine-generator systems. Goldberg and Schmus [28] demonstrated that synchronous machines may exhibit negative electrical resistance at subsynchronous frequencies, allowing electrical energy to reinforce the natural torsional vibration modes of the turbine shaft. The resulting interaction couples electrical negative resistance directly to negative effective mechanical damping, providing a practical realization of the correspondence expressed by Equation (25).

6.2. Parametric Pumping

6.2.1. Parametric Resonance and the Mathieu–Hill Instability

Periodic modulation of a system parameter transforms the governing equation into a Mathieu–Hill equation. For a mechanical oscillator with time-varying stiffness,

$$\ddot{x} + \omega_0^2\left[1 + \varepsilon \cos(\omega_p t)\right]x = 0, \tag{26}$$

where ω_0 is the natural frequency, ε is the modulation depth, and ω_p is the pump frequency. The principal parametric instability occurs when

$$\omega_p = 2\omega_0,$$

corresponding to the well-known octave relationship between the pump and the resonant mode. Under this condition, energy is transferred from the pump into the oscillation through the sidebands

$$\omega_0 \pm \frac{\omega_p}{2}.$$

The classical analysis of Mathieu–Hill stability regions, including the principal resonance and the stabilization of otherwise unstable equilibria by rapid parametric excitation, is presented by Nayfeh and Mook [29].

An important observation is that one of the canonical examples considered by Nayfeh and Mook is itself an electromechanical system: an LC resonator whose capacitance is modulated by the motion of the capacitor plates,

$$L\ddot{q} + \frac{q}{C(t)} = 0.$$

The electrical and mechanical domains are therefore coupled through the same time-dependent parameter considered in Sections 3 and 4. More recently, Kurmann [30] demonstrated that parametrically excited electrical circuits with time-varying resistance, inductance, or capacitance obey the same Mathieu–Hill dynamics as parametrically excited

mechanical oscillators. Their formulation, derived from a common Lagrangian framework, confirms the correspondence adopted in this work under the mapping

$$k \leftrightarrow \frac{1}{C}.$$

The same Floquet instability responsible for parametric resonance also underlies the band structure of periodic media, including Bloch-wave propagation in crystalline solids. Parametric resonance is therefore not restricted to either mechanical or electrical systems but represents a general property of periodically modulated linear dynamical systems.

The electrical realization of this principle is the pumped-reactance parametric amplifier introduced by Mandelstam and Papaleksi [31], in which energy is exchanged between the pump, signal, and idler frequencies. The corresponding power flow is governed by the Manley–Rowe relations [32], which establish the conservation laws for ideal parametric frequency conversion.

Parametric pumping provides the physical interpretation of time-dependent coefficients introduced in Sections 3 and 4. The parameters L, C, k, or m are not merely functions of the system state but may themselves be externally driven, thereby transferring energy into or between oscillatory modes.

This correspondence extends directly to electromechanical systems. Smith [33] analysed a pendulum coupled to an electrical resonator through a time-varying reactance and showed that the average mechanical torque follows directly from the Manley–Rowe relations. He further observed that these conservation relations apply equally to ideal lossless mechanical differentials, demonstrating that the same energy-partition principles govern both electrical and mechanical parametric interactions.

A complementary dynamical-systems formulation was developed by Holmes and Rand [34], who modelled coupled parametrically excited oscillators as interacting "motor" and "response" modes exchanging energy on a conservative manifold. Their analysis shows that nonlinear coupling ultimately limits the exponential growth predicted by the linear Mathieu equation, yielding bounded steady-state oscillations characteristic of practical parametrically excited systems.

6.2.2. Experimental Demonstration: An Autoparametric Energy Harvester

An experimentally validated realization of Equation (26) is provided by the autoparametric energy harvester developed by Kecik [35]. The device consists of a pendulum suspended from a Duffing oscillator, such that the effective pendulum stiffness is parametrically modulated by the motion of the primary oscillator. As the excitation frequency approaches the critical drive-to-natural-frequency ratio ($\vartheta \approx 0.95$), the pendulum undergoes the principal parametric instability corresponding to excitation near twice its natural frequency. The system thereby loses the stable semi-trivial equilibrium and enters the non-trivial autoparametric state, in agreement with the classical theory of autoparametric resonance [36,37]. In this regime, the dominant frequency of the primary oscillator is approximately twice that of the parametrically excited secondary oscillator.

A characteristic consequence of autoparametric resonance is the *saturation* phenomenon [37] (Section 2). Once the instability threshold is exceeded, the response amplitude of the primary oscillator remains nearly constant despite increasing excitation, while additional input energy is transferred to the parametrically excited secondary mode. Kecik [35] reported a measured reduction of approximately 25–37% in the primary vibration amplitude between the semi-trivial and non-trivial response branches, providing direct experimental evidence of this energy redistribution.

The redirected energy is subsequently converted into electrical power using an electromagnetic transducer integrated into the pendulum pivot. Maximum power generation

of approximately 0.2 W, with typical operating levels in the milliwatt range, was achieved without degrading the vibration-suppression performance of the primary oscillator. The experiment therefore demonstrates, within a single mechanical system, the essential features of parametric pumping discussed in Section 6.2: excitation near twice the natural frequency, growth of the parametrically excited mode, saturation of the primary response, and controlled transfer of energy into a secondary oscillatory subsystem.

From a broader perspective, the device represents a parametric extension of the classical dynamic vibration absorber introduced by Ormondroyd and Den Hartog [38]. The conventional absorber employs a linearly tuned auxiliary mass–spring system to divide the primary resonance into two peaks and reduce the resonant response through passive energy redistribution. Modern implementations further extend this concept using inerters and time-delay feedback [39]. In contrast, the autoparametric harvester replaces the fixed coupling with a periodically modulated one, thereby operating in the variable-coefficient regime developed throughout this paper. This parametric coupling not only suppresses the primary vibration but also redirects the transferred energy into a form that can be harvested, rather than merely dissipated.

6.2.3. Parametric Anti-Resonance and Active Stabilization

Parametric excitation is most commonly associated with destabilization through the Mathieu instability described by Equation (26). However, when the modulation frequency is tuned to a combination resonance,

$$\omega \approx \frac{\Omega_i \pm \Omega_j}{N},$$

rather than to twice the natural frequency, the same periodically varying coefficient produces the opposite effect. Instead of amplifying an oscillatory mode, it transfers energy from an unstable or weakly damped mode into a stable, positively damped mode, thereby increasing the overall damping of the system. This phenomenon is commonly referred to as *parametric anti-resonance*.

A rigorous treatment based on averaging and bifurcation analysis was presented by Fatimah and Verhulst [40], who solved the Ecker–Tondl problem for a flow-excited oscillator coupled to an absorber through a periodically varying stiffness,

$$k(t) = k_1(1 + \varepsilon \cos \omega t).$$

Their analysis demonstrated that complete suppression of the self-excited oscillation requires both positive net linear damping and an appropriate parametric excitation frequency. Furthermore, the parametric modulation significantly enlarges the parameter region in which complete suppression is achieved, with the global dynamics organized through successive Hopf, Neimark–Sacker, and torus bifurcations. Comprehensive reviews of passive absorbers, autoparametric suppression, and active parametric control are provided by Tondl [41] and by Tondl and Půst [42]. In the corresponding normal-form equations, the product of the off-diagonal coupling coefficients,

$$\frac{Q_{jk}Q_{kj}}{4\Omega_j\Omega_k},$$

appears explicitly as an additional positive damping contribution whenever its sign is positive.

The physical mechanism is a controlled transfer of modal energy. When the modulation frequency is tuned to the modal difference frequency,

$$|\omega_k - \omega_l|,$$

the pump couples the two vibration modes of the underlying linear system and periodically exchanges energy between them. In the presence of damping, this energy is preferentially redirected toward the mode with the greater dissipation, increasing the effective damping to

$$D_k + D_l\left(\frac{\omega_l}{\omega_k}\right)$$

under optimal tuning. Experimental measurements reported by Dohnal et al. [43] confirm that this mechanism produces several-fold increases in effective damping.

A particularly relevant realization is the work of Dohnal and Tondl [44], who suppressed coupled bending–torsion flutter by periodically modulating the inertia itself. Their governing equations contain a harmonically varying inertial coefficient,

$$(1 + \varepsilon \cos \omega t)\ddot{y} + \cdots,$$

corresponding directly to the variable-inertia formulation introduced in Section 4. They reported the first experimentally realizable anti-resonance based on the sum-type combination frequency,

$$\Omega_1 + \Omega_2,$$

achieving complete suppression with a modulation depth of only $\varepsilon \approx 0.06$ using out-of-phase modulation of mass and rotational inertia.

This result establishes that the variable-inertia term discussed in Section 4 is not merely a descriptive extension of the classical oscillator equations. When periodically driven, it functions as a semi-active control mechanism capable of suppressing mechanically self-excited oscillations through controlled parametric energy redistribution. Relaxing the constant-coefficient assumption therefore enables not only a more realistic mathematical description of physical systems but also practical strategies for active vibration suppression that are inaccessible within the classical constant-parameter framework.

6.3. Dynamic Coefficients as the General Oscillator Model

The developments presented in Sections 3 and 4 lead naturally to the general variable-coefficient formulation of the mechanical and electrical oscillators,

$$\frac{d}{dt}(m_{\text{eff}}(t)\dot{x}) + c(t)\dot{x} + k(t)x = F(t) \iff \frac{d}{dt}(L(t)I) + R(t)I + \frac{1}{C(t)}q = V(t). \tag{27}$$

Equation (27) represents the natural variable-coefficient extension of the classical oscillator equations. Here, $m_{\text{eff}}(t)$ denotes an effective inertial coefficient and does not, in general, imply physical mass exchange. If the coefficient variation is instead caused by actual matter entering or leaving the mechanical system, Equation (27) must be supplemented or reformulated according to the appropriate open-system momentum balance, such as the Meshchersky equation discussed in Section 4.1. The constant-coefficient models of Equations (1) and (2) are recovered when all coefficients remain constant.

7. The Inertial Element and the Equivalence Principle

The coefficient occupying the inertial position in the generalized mechanical oscillator should be interpreted as an effective inertial coefficient m_{eff}. In the special case of a rigid body undergoing translational motion without configuration-dependent or added inertial effects, m_{eff} reduces to the ordinary inertial mass m. Only in this restricted physical case is the equivalence principle directly relevant, relating inertial mass to gravitational mass. More general effective inertias arising from geometry, constraints, distributed dynamics, fluid added mass, or controlled inertial mechanisms should not be identified with gravitational

mass. The mechanical energy-storage element nevertheless occupies the $\alpha = +1$ position of the generalized fractional-order representation in Equation (20).

8. A Falsifiable Prediction

The unified formulation presented in this work yields experimentally testable predictions rather than serving solely as a descriptive analogy. In a doubly state-dependent oscillator driven parametrically according to Equation (26), the exchange of power among the pump, signal, and idler frequencies must satisfy the Manley–Rowe relations. Consequently, no passive lossless system based solely on variable reactances can exceed the corresponding frequency-conversion limit.

This limitation is not restricted to electrical circuits. Penfield and Rafuse [45] (Section 2.1) showed that the Manley–Rowe relations apply to any lossless nonlinear reactive element, including rotating electrical machines, conservative electromechanical transducers, and ideal acoustic systems. The same power-conservation constraint therefore applies equally to mechanical systems employing variable inertia or stiffness and to electrical systems employing variable inductance or capacitance. Dissipative elements, such as viscous dampers or electrical resistance, necessarily reduce the attainable conversion efficiency below the lossless limit.

The Manley–Rowe relations complement the classical energy interpretation introduced through the quality factor in Section 2. The quality factor distinguishes between reactive energy, which is periodically stored and returned to the system, and resistive energy, which is irreversibly dissipated. The Manley–Rowe relations further demonstrate that, in an ideal lossless parametric device, reactive energy is redistributed among frequency components while remaining globally conserved. Energy leaves the system only through dissipative mechanisms.

This interpretation is consistent with the two-signed reactive-energy formulation proposed by Naan [46], in which the net reactive-energy balance remains identically zero. Although this viewpoint provides useful physical intuition, the conclusions of the present section rely solely on the established quality-factor formulation and the Manley–Rowe conservation laws.

For a specific device, the Manley–Rowe relations provide a quantitative upper bound. Consider a lossless parametric up-converter employing a single variable reactance, where the output frequency is

$$\omega_o = \omega_s + \omega_p.$$

The maximum achievable power gain is then

$$\left(\frac{P_o}{P_s}\right)_{\max} = \frac{\omega_o}{\omega_s}, \tag{28}$$

as established in the classical theory of parametric frequency conversion [45,47]. For example, a varactor up-converter driven with

$$\omega_p = 9\omega_s$$

is fundamentally limited to a power gain of

$$\frac{\omega_o}{\omega_s} = 10,$$

corresponding to approximately 10 dB, consistent with the dynamic behaviour analysed by Brady [48].

Equation (28) provides a direct experimental criterion for validating the passive parametric model. A calorimetric energy balance performed on a parametrically driven variable-reactance or variable-inertia device should satisfy the Manley–Rowe limit within experimental uncertainty. Measured performance exceeding this theoretical bound would falsify the passive parametric description, whereas agreement with or below the predicted limit would support the unified model presented in this work.

9. Proposed Experimental Validation of the Unified Parametric Framework

The theoretical developments presented in Sections 2–8 lead naturally to an experimental validation. Rather than comparing separate mechanical and electrical test rigs, a single electromechanical system is proposed in which both domains interact through a common time-varying parameter. Parametric excitation is chosen as the experimental mechanism because it represents the direct physical realization of the state-dependent coefficients introduced in Sections 3 and 4. The objective is to test the proposed unified second-order structure within a single experimental platform.

9.1. Experimental Configuration

The proposed apparatus consists of an electromechanical resonator in which a deliberately time-varying reactance couples a mechanical mode to an electrical mode. The concept follows the electromechanical Manley–Rowe system analysed by Smith [33]. A mechanical resonator with natural frequency ω_{mech} modulates an electrical reactance, implemented either as a variable capacitor or as a saturable-core inductor, which forms one branch of an electrical resonator with natural frequency ω_{elec}. The shared reactance is driven by an external pump operating at frequency ω_p.

Because both measurement ports are coupled through the same time-dependent coefficient, the electrical and mechanical responses are expected to satisfy the same conservation relations derived in Section 5 and Domain-Independent Interpretation: The Metriplectic Formulation. The proposed configuration therefore permits simultaneous validation of the theoretical framework in both physical domains.

9.2. Experimental Predictions

The proposed experiment yields three independently testable predictions.

1. Principal parametric resonance.
   When the pump frequency is swept, the equilibrium state is predicted to lose stability near
   $$\omega_p = 2\omega_0,$$
   with sideband generation at
   $$\omega_0 \pm \frac{\omega_p}{2},$$
   consistent with the classical Mathieu–Hill instability discussed in Section 6.2.1 [29]. Because both measurement ports observe the same parametrically excited system, the instability threshold should occur at the same pump frequency in both the mechanical and electrical measurements. A systematic discrepancy between the two domains would contradict the proposed unified description.
2. Common Manley–Rowe limit.
   Operating the apparatus as a parametric up-converter,
   $$\omega_s \to \omega_o = \omega_s + \omega_p,$$

the power conversion efficiency is predicted to satisfy the Manley–Rowe limit,

$$\left(\frac{P_o}{P_s}\right)_{\max} = \frac{\omega_o}{\omega_s},$$

given by Equation (28). The corresponding partition of energy between the electrical and mechanical subsystems should follow the same conservation law, consistent with the electromechanical analysis of Smith [33]. Measured performance exceeding the Manley–Rowe limit or inconsistent energy partitioning between the two domains would falsify the passive parametric model presented in Section 8.

3. Parametric anti-resonance.
   Retuning the pump frequency to the modal combination frequency,

$$|\omega_{\text{mech}} - \omega_{\text{elec}}|,$$

is predicted to increase the effective damping through parametric anti-resonance, approaching the theoretical limit

$$D_k + D_l\left(\frac{\omega_l}{\omega_k}\right)$$

under optimal tuning [43]. When implemented through periodic modulation of inertia rather than stiffness, the same apparatus should reproduce the flutter-suppression mechanism demonstrated by Dohnal and Tondl [44], including suppression at modulation depths as small as

$$\varepsilon \approx 0.06.$$

For reference, experimentally demonstrated autoparametric harvesters operating on the same physical principle have achieved electrical output powers approaching

$$P_{\max} \approx 0.2 \text{ W},$$

with typical operating powers in the milliwatt range while maintaining effective vibration suppression [35]. No quantitative performance is claimed here; the three measurements listed above constitute experimentally testable predictions whose outcomes are constrained by the theoretical limit of Equation (28).

From a broader energy-harvesting perspective, the present parametric energy-transfer framework can be interpreted as a resonant energy-conversion mechanism whose practical role is analogous to other harvesting architectures: energy available in an external physical degree of freedom is coupled into an electrical subsystem through a deliberately engineered transduction process. Contemporary energy-harvesting systems commonly exploit electromagnetic, mechanical, thermal, optical, or radio-frequency energy and combine the transducer with appropriate power-management and energy-storage stages in order to accommodate the intermittent and time-varying nature of the available source [49]. In this context, the distinctive feature of the present approach is that the energy-transfer pathway is governed by a shared time-varying system parameter and by the resulting parametric and combination-frequency interactions. Rather than relying solely on direct linear transduction at a single forcing frequency, the proposed structure provides a mechanism by which energy present in one dynamical mode or frequency band can be transferred into another mode through controlled modulation of the system coefficients. This places the method conceptually within the wider class of resonant and nonlinear energy-harvesting techniques, while emphasizing frequency conversion, modal coupling, and parametric amplification as the principal mechanisms governing the transfer. As in conventional harvesting systems, any claim of net harvested electrical energy ultimately requires a complete power

balance that includes the excitation or pumping power, conversion losses, conditioning electronics, and delivered load power; nevertheless, the theoretical framework developed here provides a structured basis for designing and experimentally evaluating such resonant harvesting configurations.

9.3. Experimental Apparatus

The specific implementation of the proposed apparatus—including the mechanical resonator, operating frequency range, variable reactance technology, pump source, instrumentation, and power-measurement methodology—may be selected according to practical design considerations. The theoretical framework developed in this paper requires only three structural properties: a single shared time-varying coefficient, simultaneous electrical and mechanical observation ports, and operation in both the principal parametric-resonance and combination-frequency regimes. Any experimental realization satisfying these conditions provides a suitable platform for testing the proposed unified model.

10. Experimental Results

The preceding sections established the theoretical framework of the proposed unified electromechanical oscillator, extending the classical constant-coefficient analogy to systems with state-dependent parameters, parametric excitation, and active energy transfer. The analysis further identified experimentally testable predictions, including the occurrence of principal parametric resonance, the applicability of the Manley–Rowe power-conservation relations, and the stabilizing effect of parametric anti-resonance.

This section presents the experimental realization used to evaluate these predictions. The measurements were performed on a resonant Metglas AMCC-1000 paraformer prototype designed to exhibit the coupled electromechanical behaviour developed throughout this work [2]. The experimental results are organized to progress from the physical implementation and measured electrical characteristics to resonance behaviour, numerical simulations, and optimization studies. Together, these measurements provide an experimental assessment of the proposed unified variable-coefficient framework and its applicability to practical resonant energy-transfer systems.

10.1. Device and Winding Description

The experimental magnetic assembly is based on a Metglas/Powerlite AMCC-1000 cut core manufactured from amorphous 2605SA1 alloy [2]. The nominal net core cross-sectional area is $A_e = 23.0\ \mathrm{cm}^2$ and the nominal magnetic path length used in the present first-order calculations is $\ell_e = 42.7$ cm. The material saturation flux density is approximately $B_s = 1.56$ T. The permeability is not treated as a fixed material constant because the magnetic reluctance is governed predominantly by the two cut interfaces, their insulation layers, mechanical pressure, residual surface roughness, and fringing.

The output resonator consists of two nominally symmetric windings, denoted L2a and L2b. Each winding is made from approximately 7 m of 1000/38 Litz conductor, i.e., 1000 strands with an individual strand diameter of approximately 0.1 mm. Each winding contains approximately 14.5 turns on one core leg. The measured small-signal inductance of one branch, with the capacitors disconnected and with the other windings physically installed, is

$$L_{2,\mathrm{meas}} = 1405\ \mu\mathrm{H}. \tag{29}$$

as shown in Figure 1.

Each branch is shunted by a nominal 100 nF, 1000 VRMS, 350 ARMS high-current resonant capacitor [50]. The centre ends of L2a and L2b are connected to the common

reference node, whereas the outer ends feed separate rectifier diodes. Thus, each half winding and its local shunt capacitor form a branch resonator referenced to the centre tap.



Figure 1. Prototype Metglas/Powerlite AMCC-1000 with Litz wires.

The pump winding L1 is made from approximately 28 m of 1500/44 Litz conductor, corresponding to 1500 strands of approximately 0.05 mm diameter. The intended pump capacitor is an ASC X675 metallized-polyester capacitor rated at 6000 VDC with a nominal capacitance of 0.047 µF = 47 nF [51]. The pump is to be tuned near 32 kHz, twice the intended 16 kHz output frequency.

Two layers of iFixit polyimide tape are placed at each mating interface of the U-shaped core halves. The iFixit product page identifies the tape as compatible with KPT-1/2-type polyimide tape. A commercially listed KPT-1/2 equivalent has a total thickness of approximately 0.064 mm per layer, including approximately 0.025 mm polyimide backing and 0.038 mm silicone adhesive. Because the exact lot and compressed thickness have not been measured, the present model treats the tape thickness as an uncertain parameter. With two layers at each of two magnetic joints, the nominal geometric tape contribution is approximately

$$g_{\mathrm{tape,nom}} = 2\ (\mathrm{joints}) \times 2\ (\mathrm{layers/joint}) \times 0.064\ \mathrm{mm} = 0.256\ \mathrm{mm}. \tag{30}$$

This value is not identical to the effective magnetic gap because adhesive compression, surface waviness, residual air pockets, and fringing alter the reluctance.

10.2. Inductance and Resonance Equations

For a magnetic circuit with a core reluctance and a total gap reluctance,

$$\mathcal{R}_{\mathrm{m}} = \frac{\ell_{\mathrm{e}}}{\mu_0 \mu_{\mathrm{r}} A_{\mathrm{e}}} + \frac{g_{\mathrm{eff}}}{\mu_0 A_{\mathrm{e,fr}}}, \tag{31}$$

where $A_{\mathrm{e,fr}}$ is an effective fringing-corrected gap area. The winding inductance is

$$L = \frac{N^2}{\mathcal{R}_{\mathrm{m}}}. \tag{32}$$

When the gap reluctance dominates,

$$L \approx \frac{\mu_0 N^2 A_{\mathrm{e}}}{g_{\mathrm{eff}}}, \qquad g_{\mathrm{eff}} \approx \frac{\mu_0 N^2 A_{\mathrm{e}}}{L}. \tag{33}$$

The measured inductance also defines the experimental A_L value,

$$A_{L,\mathrm{meas}} = \frac{L_{2,\mathrm{meas}}}{N_2^2} = 6.682\ \mu\mathrm{H\,turn^{-2}}. \tag{34}$$

Equation (33), using $A_e = 23\ \mathrm{cm}^2$, $N_2 = 14.5$, and $L_{2,\mathrm{meas}} = 1405\ \mu\mathrm{H}$, gives an equivalent total gap of

$$g_{\mathrm{eff}} \approx 0.433\ \mathrm{mm}. \tag{35}$$

The difference between 0.433 mm and the nominal tape-stack value of 0.256 mm is physically plausible and represents residual mechanical gap, adhesive compliance, nonuniform contact, and the limitations of the gap-dominated approximation.

The ideal resonance frequency of a branch is

$$f_0 = \frac{1}{2\pi\sqrt{LC}}. \tag{36}$$

For the measured 1405 µH and 100 nF,

$$f_{2,\mathrm{present}} = \frac{1}{2\pi\sqrt{(1405\ \mu\mathrm{H})(100\ \mathrm{nF})}} = 13.429\ \mathrm{kHz}. \tag{37}$$

Therefore, the measured branch does *not* resonate at 16 kHz with a 100 nF capacitor. Exact 16 kHz tuning requires either

$$L_{2,\mathrm{target}} = \frac{1}{(2\pi 16\ \mathrm{kHz})^2(100\ \mathrm{nF})} = 989.46\ \mu\mathrm{H}, \tag{38}$$

$$C_{2,\mathrm{target}} = \frac{1}{(2\pi 16\ \mathrm{kHz})^2(1405\ \mu\mathrm{H})} = 70.42\ \mathrm{nF}. \tag{39}$$

The value $L_{2,\mathrm{target}} = 989.46\ \mu\mathrm{H}$ should be regarded as a *preliminary tuning target* obtained from the ideal uncoupled LC relation, rather than as the final in-circuit inductance, because the effective resonance is modified by winding geometry, mutual coupling, parasitic reactances, and the complete assembled circuit.

If the effective gap remains unchanged and $L \propto N^2$, the approximate winding target is

$$N_{2,\mathrm{target}} = 14.5\sqrt{\frac{989.46}{1405}} = 12.17\ \mathrm{turns}. \tag{40}$$

Because fractional turns, lead inductance, mutual coupling, and rectifier capacitance affect the final value, a practical target is 12 turns plus a removable trim loop or a switched capacitor bank.

For the pump branch with $C_1 = 47$ nF at 32 kHz,

$$L_{1,\mathrm{target}} = \frac{1}{(2\pi 32\ \mathrm{kHz})^2(47\ \mathrm{nF})} = 526.32\ \mu\mathrm{H}. \tag{41}$$

This is the required *final measured in-circuit inductance*; it cannot be inferred reliably from the 28 m conductor length alone because the turn count, winding position, orthogonal magnetic coupling, and installed L2 windings determine the result.

Centre-Tapped Two-Winding Modes

The two output windings form a coupled system with self-inductances L_{2a} and L_{2b} and mutual inductance $M = k\sqrt{L_{2a}L_{2b}}$. For the symmetric case $L_{2a} = L_{2b} = L_2$, the two linear modal inductances are

$$L_+ = L_2 + M = L_2(1+k), \qquad L_- = L_2 - M = L_2(1-k), \tag{42}$$

and, for equal branch capacitors,

$$f_{\pm} = \frac{1}{2\pi\sqrt{L_2(1 \pm k)C_2}}. \tag{43}$$

Consequently, the measured single-branch inductance alone is insufficient to predict the centre-tapped modal frequencies. The coupling coefficient and winding polarity must be measured. A four-terminal impedance measurement should determine L_{2a}, L_{2b}, the series-aiding inductance L_{aid}, and the series-opposing inductance L_{opp}:

$$M = \frac{L_{\text{aid}} - L_{\text{opp}}}{4}, \tag{44}$$

$$k = \frac{M}{\sqrt{L_{2a}L_{2b}}}. \tag{45}$$

The 16 kHz target must then be assigned to the actual mode excited by the rectifier and load, not merely to the isolated winding value.

10.3. Parametric-Excitation Condition

A first-order representation of the output coordinate $q(t)$ is the damped Mathieu equation

$$\ddot{q} + \frac{\omega_0}{Q_2}\dot{q} + \omega_0^2\left[1 + h\cos(\omega_p t)\right]q = 0, \tag{46}$$

where $\omega_0 = 2\pi f_2$, $\omega_p = 2\pi f_p$, Q_2 is the loaded output quality factor, and h is the fractional modulation depth of the effective stiffness, inductance, or reluctance. The principal parametric condition is

$$f_p \approx 2f_2. \tag{47}$$

Thus, 32 kHz pumping and 16 kHz output resonance satisfy the principal 2:1 condition. Near exact tuning, a commonly used small-signal threshold estimate is

$$h_{\text{th}} \approx \frac{2}{Q_2}. \tag{48}$$

This equation does not prove that the present magnetic geometry produces sufficient modulation. The modulation depth must be extracted experimentally from the pump-dependent incremental inductance or from sideband measurements.

10.4. Simulation Results

Figure 2 shows the direct consequence of Equation (36). The present 1405 µH/100 nF branch lies at 13.429 kHz; the 16 kHz target corresponds to 989.46 µH. Figure 3 illustrates the strong gap sensitivity of the gap-dominated model. The inferred effective gap is approximately 0.433 mm, whereas the nominal uncompressed four-layer tape contribution is approximately 0.256 mm.

Figure 4 demonstrates that mutual coupling can split the two output resonances substantially. Hence, the loaded centre-tapped assembly must be characterized as a two-port coupled resonator. Figure 5 gives the approximate first-tongue modulation threshold, and Figure 6 provides an illustrative linear Mathieu simulation. These simulations establish tuning and stability requirements; they do not predict power gain without measured nonlinear permeability, loss, coupling, and diode-load data.

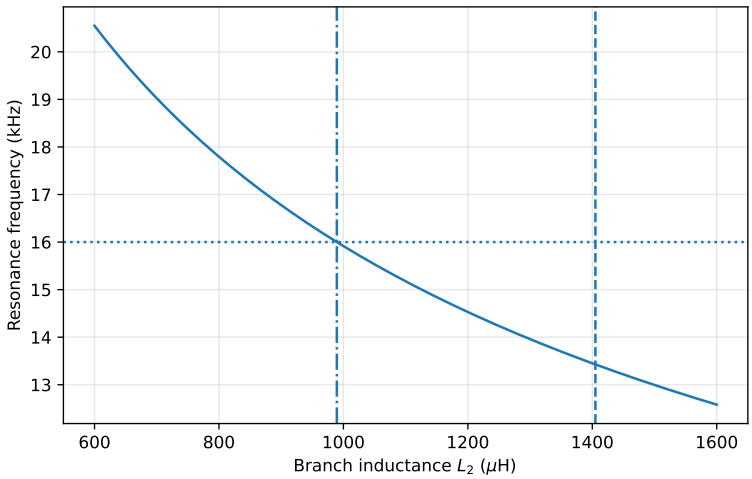


Figure 2. Branch resonance frequency as a function of inductance for $C_2 = 100$ nF. The present 1405 µH/100 nF branch lies at 13.429 kHz (dashed line) and the 16 kHz target corresponds to 989.46 µH (dash-dotted line).

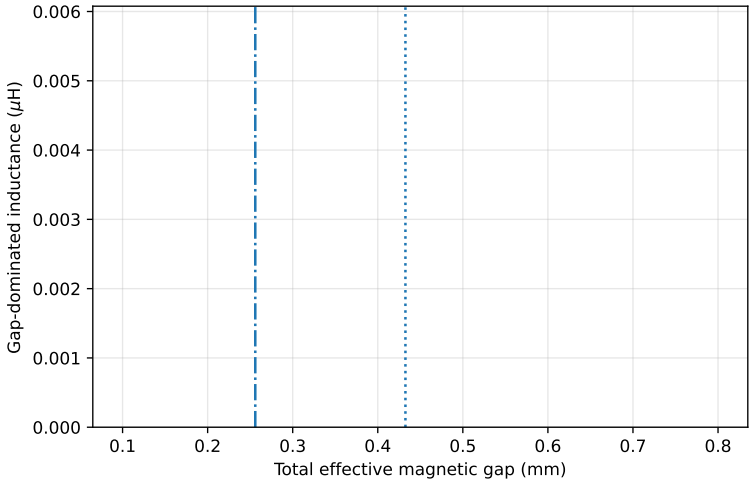


Figure 3. Gap-dominated inductance estimate for the AMCC-1000 cross-sectional area and 14.5 turns. The inferred effective gap is approximately 0.433 mm (dotted line), whereas the nominal uncompressed four-layer tape contribution is approximately 0.256 mm (dash-dotted line).

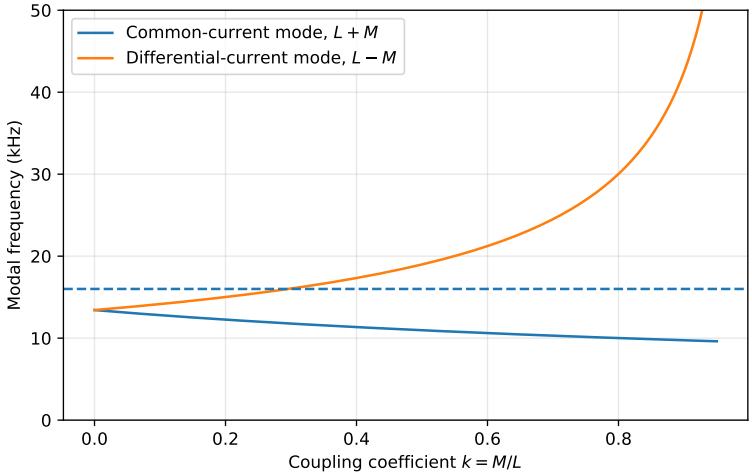


Figure 4. Common-current and differential-current modal frequencies versus coupling coefficient for $L_2 = 1405$ µH and $C_2 = 100$ nF. The target frequency of 16 kHz is marked with a dashed line.

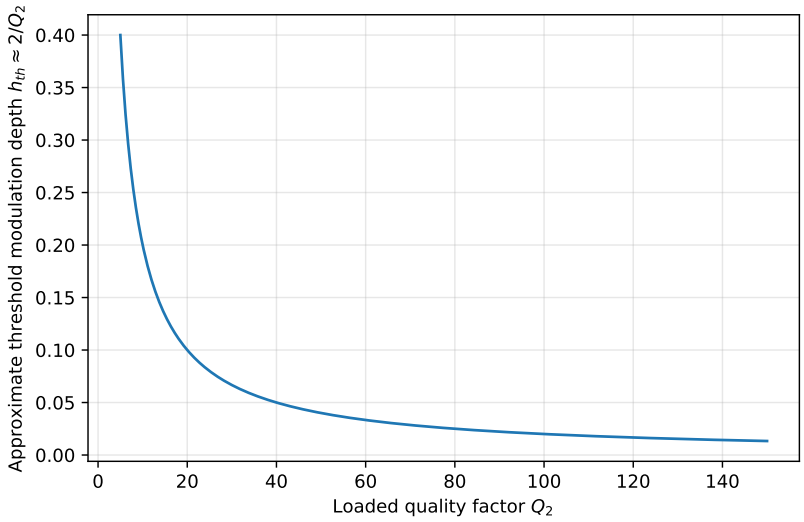


Figure 5. Approximate threshold modulation depth for principal parametric excitation.

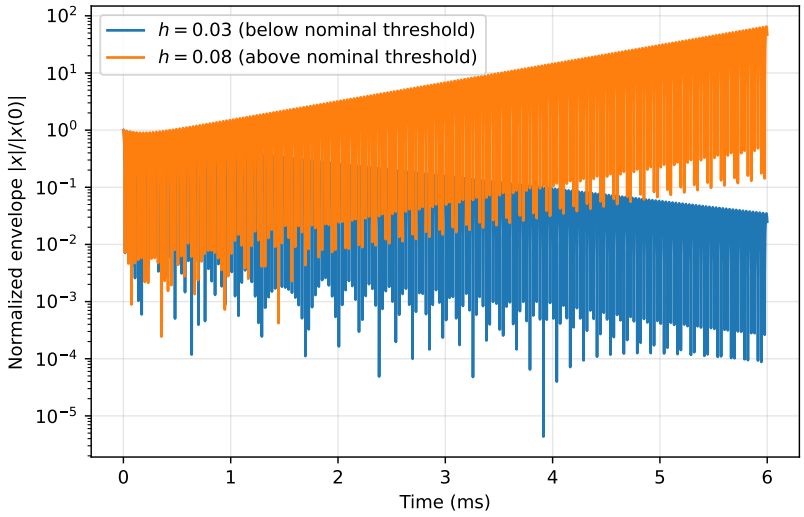


Figure 6. Illustrative Mathieu-equation response below and above the nominal threshold for $Q_2 = 40$.

10.5. Fine-Tuning Plan for the Final Experiments

The final experimental campaign should begin with a direct mechanical characterization of the assembled AMCC-1000 core. The compressed tape stack should be measured with a micrometer at multiple locations, recording both the free tape thickness and the clamped joint thickness. Catalogue values should not be substituted for these measurements. After the windings have been installed, but before connecting capacitors or rectifiers, the inductances L_{2a}, L_{2b}, L_{aid}, and L_{opp}, together with the winding resistances and impedance phase, should be measured over the frequency range from 1 kHz to at least 100 kHz. These measurements provide the mutual inductance, coupling coefficient, and frequency-dependent losses required for the subsequent tuning procedure.

The output branches should initially be tuned without the rectifier. With fixed 100 nF capacitors, the target branch or modal inductance is approximately 989.5 µH. Reversible adjustments, such as removable fractional turns, a small series air-core trimming inductor, or a parallel capacitor bank covering approximately 60 nF to 100 nF, are preferred to irreversible winding modifications. After reconnecting the centre tap, the modal frequencies should be measured and the mode corresponding to the intended winding polarity and rectifier conduction sequence should be tuned to 16.000 kHz, rather than tuning the isolated branches individually.

The input resonator should then be completed by installing the L1 winding and adjusting its in-circuit inductance to approximately 526.3 µH with the 47 nF ASC capacitor. Initial measurements should be performed at low excitation levels. Since the X675 capacitor rating refers to DC operation, its repetitive AC current capability at 32 kHz should be verified experimentally from the temperature rise, dissipation factor, and available manufacturer data.

Finally, the influence of increasing excitation should be characterized by measuring $L_1(V,I)$, $L_2(V,I)$, resonance frequency, phase, harmonic content, and core temperature. The manufacturer-supplied core-loss relation,

$$P_{\text{core}}[\text{W/kg}] \approx 6.5 f[\text{kHz}]^{1.51} B[\text{T}]^{1.74}, \tag{49}$$

should be applied only within its validated flux-density range and with the measured waveform and thermal conditions. Parametric excitation should then be investigated by sweeping the pump frequency through approximately 30 kHz to 34 kHz while monitoring the 16 kHz component. The onset of parametric operation should be confirmed by observing a distinct threshold, frequency locking, sideband generation, and the associated redistribution of energy.

10.6. Conclusions of the Experimental Tests

The measured 1405 µH inductance is internally consistent with an experimental A_L value of 6.682 µH turn^{-2} and an effective total magnetic gap of approximately 0.433 mm in a gap-dominated model. However, it yields an isolated branch resonance of only 13.429 kHz with 100 nF. Exact 16 kHz tuning requires approximately 989.46 µH per relevant branch/mode, or alternatively 70.42 nF at the measured inductance. The 32 kHz pump branch requires an in-circuit inductance of approximately 526.32 µH with the 47 nF ASC X675 capacitor.

The 2:1 frequency relation is a necessary but not sufficient condition for parametric resonance. The final claim must be supported by measurements of mutual coupling, loaded quality factors, pump-induced inductance modulation, parametric threshold, phase locking, and complete real-power balance. The supplied Python 3.10, MATLAB R2025b, and Wolfram Language 14.0.0.0 scripts reproduce the numerical results and figures and can be updated directly when the review measurements become available.

10.7. Optimized 32 kHz-to-16 kHz Fine-Tuning Plan

10.7.1. Optimization Objective and Nominal Targets

The optimized design objective is to realize the principal parametric relation

$$f_1 = 2f_2, \qquad f_1 = 32.000\ \text{kHz}, \qquad f_2 = 16.000\ \text{kHz}, \tag{50}$$

after all windings, capacitors, rectifier diodes, measurement leads, and the intended load have been installed. The optimization must therefore be applied to the *measured in-circuit modal inductances*, not to isolated winding estimates.

For the output capacitance $C_2 = 100$ nF, the required relevant output-mode inductance is

$$L^{\star}_{2,\text{mode}} = \frac{1}{(2\pi 16\ \text{kHz})^2 100\ \text{nF}} = 989.465\ \mu\text{H}. \tag{51}$$

For the pump capacitance $C_1 = 47$ nF, the required in-circuit pump inductance is

$$L^{\star}_{1} = \frac{1}{(2\pi 32\ \text{kHz})^2 47\ \text{nF}} = 526.311\ \mu\text{H}. \tag{52}$$

If the present gap and winding geometry remain unchanged, the output winding estimate based on $L \propto N^2$ is

$$N^{\star}_{2} = 14.5\sqrt{\frac{989.465}{1405}} = 12.168\ \text{turns}. \tag{53}$$

Thus, 12 turns with a reversible fractional-turn or capacitor trim is the recommended starting point. This is not a substitute for the coupled-mode measurement.

10.7.2. Coupling-Aware Target

For equal output windings with self-inductance L_s and coupling coefficient k, the two modal inductances are

$$L_+ = L_s(1+k), \qquad L_- = L_s(1-k). \tag{54}$$

Consequently, the self-inductance required for a 16 kHz mode is

$$L_s^\star = \frac{L_{2,\mathrm{mode}}^\star}{1 \pm k}. \tag{55}$$

The plus sign applies to the common-current or series-aiding mode and the minus sign to the differential-current or series-opposing mode. Figure 7 shows that even moderate coupling changes the branch target substantially. Therefore, the final optimization sequence must first identify the mode excited by the diode polarity and centre-tapped connection.

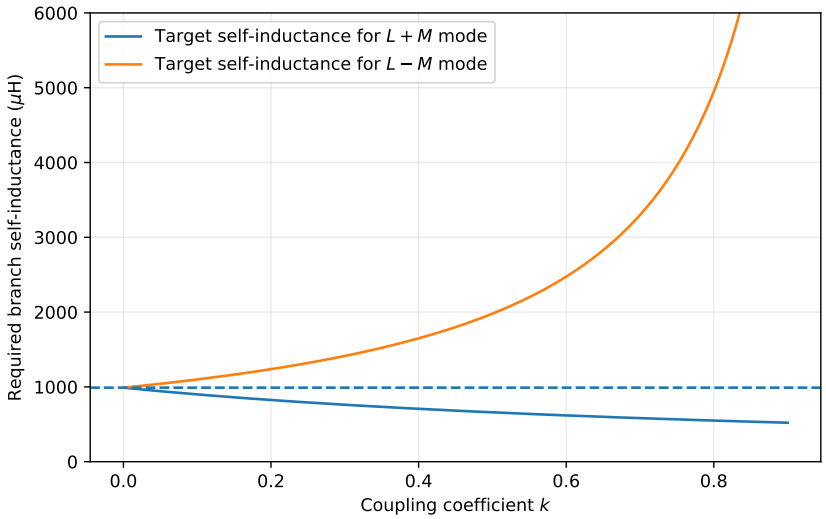


Figure 7. Required branch self-inductance for a 16 kHz coupled mode as a function of the measured coupling coefficient. The dashed-line indicated and inductance of 989.465 µH.

10.7.3. Discrete Winding and Capacitor Trim

A practical tuning study was performed using quarter-turn winding increments and commercially available capacitor values. Assuming the local scaling relation $L \propto N^2$, the optimum configuration near the preferred branch capacitance of 100 nF corresponds to approximately 12.25 turns, as shown in Figure 8. Because the effective inductance is influenced by lead routing, mutual coupling, tape compression, and the presence of the L1 winding, the calculated value should be regarded only as an initial estimate.

The preferred implementation is therefore to wind 12 complete turns while retaining an accessible half-turn or quarter-turn trimming conductor. Fine adjustment should be achieved with a low-inductance capacitor bank covering approximately 68 nF to 110 nF. Resonance should always be adjusted using the complete centre-tapped output mode rather than the disconnected individual branches, and the L1 resonator should be tuned only after the L2 assembly has reached its final mechanical and electrical configuration.

10.8. Robustness and Tolerance Simulation

A Monte Carlo simulation with 10^5 samples was conducted around the optimized targets. The assumed post-trim standard deviations were 0.5% for the measured inductances

and 0.3% for the effective capacitances. These values are engineering assumptions for planning and must be replaced with measured repeatability and component-temperature data in the final article.

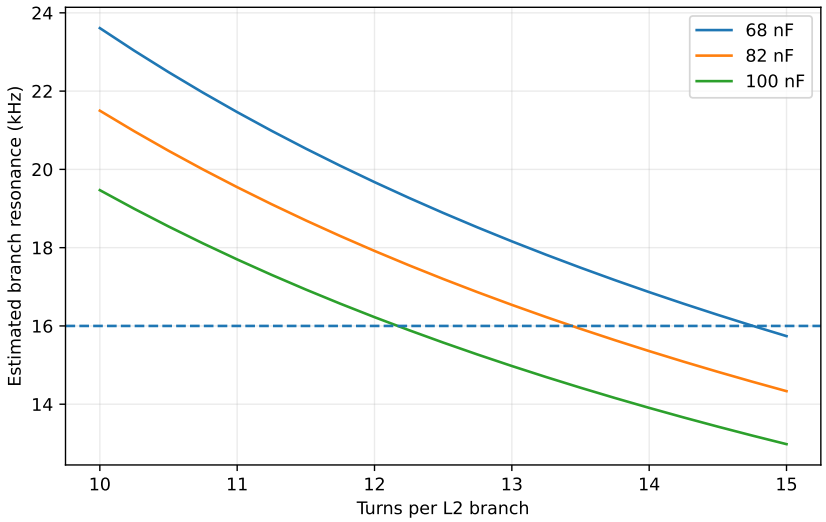


Figure 8. Estimated output resonance versus L2 turns for representative capacitor values. The curves use the measured 1405 µH at 14.5 turns as the local calibration point. The target frequency of 16 kHz is marked with a dashed line.

The simulated output-frequency mean was 16,000.04 Hz with a standard deviation of 46.80 Hz, as shown in Figure 9. The central 95% interval was 15,908.3 Hz to 16,092.2 Hz. The pump-to-output frequency ratio had a mean of 2.000041 and a standard deviation of 0.008270, as illustrated in Figure 10. These results indicate that independent trimming of both tanks is required; nominal components alone are insufficient for a repeatable 2:1 relationship.

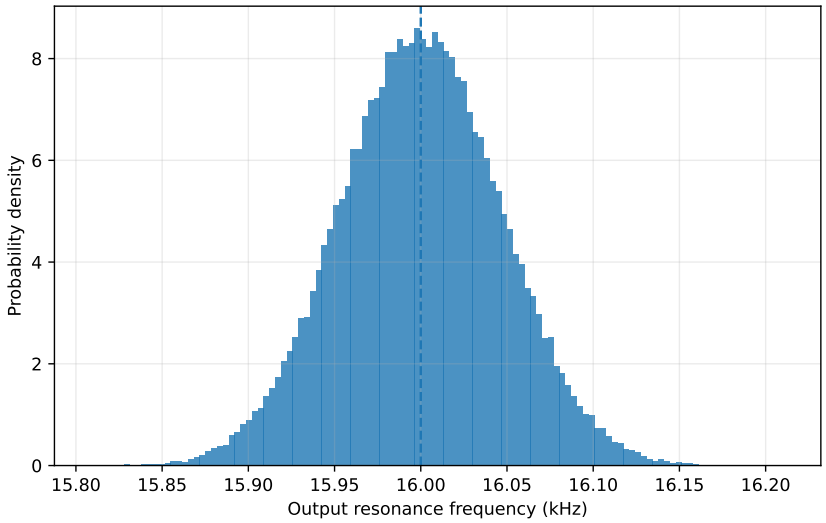


Figure 9. Monte Carlo distribution of the output resonance after nominal tuning to 16 kHz. The target frequency of 16 kHz is marked with a dashed line.

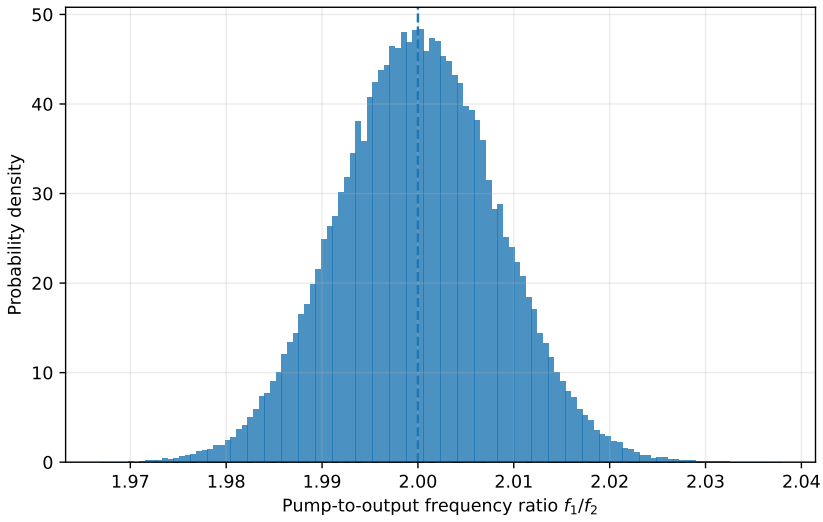


Figure 10. Monte Carlo distribution of the pump-to-output frequency ratio. The target frequency ratio of 2 is marked with a dashed line.

10.8.1. Parametric Threshold and Detuning

For the principal Mathieu instability tongue, a useful first-order boundary including output detuning is

$$h_{\text{th}} \approx 2\sqrt{\left(\frac{1}{Q_2}\right)^2 + \left(\frac{2\Delta f_2}{f_2}\right)^2}, \tag{56}$$

where h is the effective fractional modulation depth and Δf_2 is the output detuning from half the pump frequency. At exact tuning, this reduces to $h_{\text{th}} \approx 2/Q_2$. For example, $Q_2 = 40$ gives a nominal threshold of approximately 0.05, whereas $Q_2 = 80$ gives approximately 0.025. Rectifier conduction and load current reduce the loaded Q_2 and therefore increase the required pump-induced modulation (Figure 11).

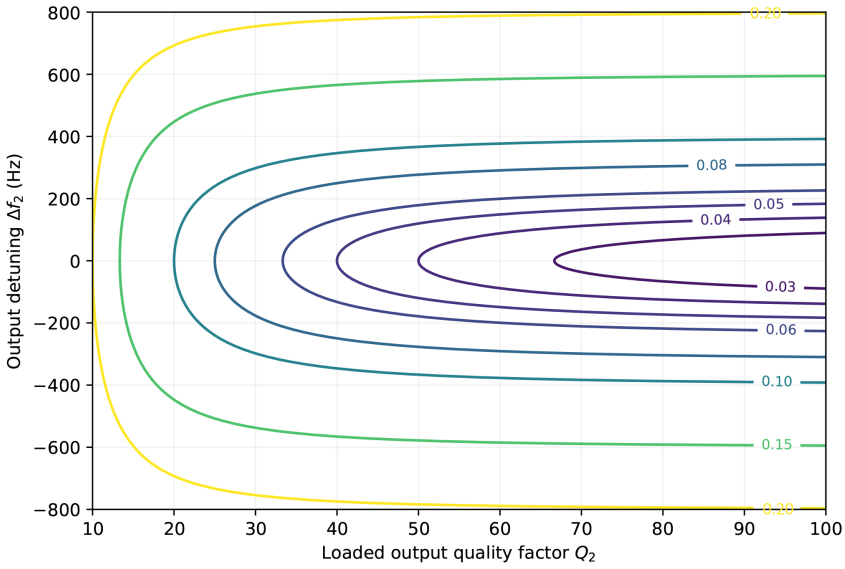


Figure 11. Approximate parametric-instability threshold as a function of loaded quality factor and output-frequency detuning. Contour values denote the required modulation depth h_{th}.

10.8.2. Final Optimized Experimental Sequence

The experimental procedure should follow a well-defined sequence to minimize ambiguity and to distinguish genuine parametric excitation from ordinary forced res-

onance. The measurements should begin with a mechanical baseline characterization of the AMCC-1000 assembly by clamping the core halves with a repeatable torque, measuring the compressed joints, and repeating the assembly several times to quantify mechanical repeatability.

Electrical characterization should then be performed with the L1 winding installed but open-circuited and with all capacitors and rectifiers disconnected. The inductances L_{2a}, L_{2b}, L_{aid}, and L_{opp}, together with the winding resistance and impedance phase, should be measured to determine the mutual inductance and coupling coefficient. The winding polarity should subsequently be verified to identify whether the rectifier excites the $L + M$ or $L - M$ mode, allowing the corresponding branch inductance target to be calculated.

The output resonator should first be adjusted by reversible changes to the L2 windings until the unloaded modal frequency lies within approximately 200 Hz of 16 kHz. Fine tuning should then be completed with the capacitor bank so that the fully assembled and loaded output mode resonates at exactly 16.000 kHz. After connecting the rectifier and the intended load, the resonance frequency and phase should be remeasured because junction capacitance and conduction intervals modify both the resonance condition and the effective damping.

The pump resonator should then be completed by connecting the 47 nF X675 capacitor and adjusting the measured L1 inductance to approximately 526.311 µH, thereby tuning the pump circuit to 32.000 kHz with the final output configuration in place. Parametric excitation should first be investigated at low voltage by sweeping the pump frequency through approximately 31 kHz to 33 kHz while recording the output spectrum, pump sidebands, phase response, and input and output power. The excitation amplitude should subsequently be increased in small increments to determine the onset threshold of the 16 kHz oscillation and to verify the characteristic signatures of parametric resonance.

10.8.3. Optimized Numerical Recommendation

Before the coupled-mode measurements are available, the recommended nominal starting point is:

$$C_1 = 47\ \mathrm{nF}, \qquad L_1^{\star} = 526.311\ \mu\mathrm{H}, \qquad f_1 = 32.000\ \mathrm{kHz}, \tag{57}$$

$$C_2 = 100\ \mathrm{nF\ per\ branch}, \qquad L_{2,\mathrm{mode}}^{\star} = 989.465\ \mu\mathrm{H}, \qquad f_2 = 16.000\ \mathrm{kHz}. \tag{58}$$

The approximate winding start value is 12 turns per L2 branch with reversible trim. The value 989.465 µH is a *modal target*. It must not be assigned blindly to the isolated branch if the measured coupling coefficient is appreciable.

11. Final Real Experimental Tests

11.1. Direct Time-Domain and Spectral Validation of the 2:1 Resonant Operating Point

The final bench measurement was performed with the completed resonant magnetic assembly and the component values obtained from the preceding analytical and numerical design procedure. The primary resonator used $L_1 = 262.9\ \mu\mathrm{H}$ and $C_1 = 0.094\ \mu\mathrm{F}$ (two 47 nF ASC capacitors in parallel), while both secondary branches used $L_{2a} = L_{2b} = 934.8\ \mu\mathrm{H}$ and $C_{2a} = C_{2b} = 0.1\ \mu\mathrm{F}$. From the same resonance relation used in the theoretical development,

$$f_0 = \frac{1}{2\pi\sqrt{LC}}, \tag{59}$$

the corresponding uncoupled tuning frequencies are

$$f_1 = \frac{1}{2\pi\sqrt{L_1 C_1}} = 32.016 \text{ kHz}, \tag{60}$$

$$f_{2a} = f_{2b} = \frac{1}{2\pi\sqrt{L_2 C_2}} = 16.461 \text{ kHz}. \tag{61}$$

Their ratio is $f_1/f_2 = 1.9449$, i.e., within approximately 2.75% of the ideal 2:1 relation required by the parametric-excitation mechanism developed in the preceding theory sections. Thus, the final measured component set realizes the intended approximately 32 kHz pump resonance and approximately 16 kHz secondary resonance directly from the physical component values.

Figure 12 shows the simultaneously acquired oscilloscope channels from `SDS00001.DAT`. One side of the magnetic structure was observed with the voltage probe (CH1), whereas the other side was observed through the RF current probe (CH3).

The RF current-probe conversion is $V/0.84\ \Omega$ for 16 kHz and $V/2.26\ \Omega$ for 32 kHz.

The record contains 140,000 samples at a 1 ns sampling interval, corresponding to a 1 GSa s^{-1} acquisition rate and a 140 µs observation interval. The simultaneous voltage- and current-probe waveforms show a repeatable resonant structure throughout the captured interval, consistent with coupled resonant operation predicted by the model.

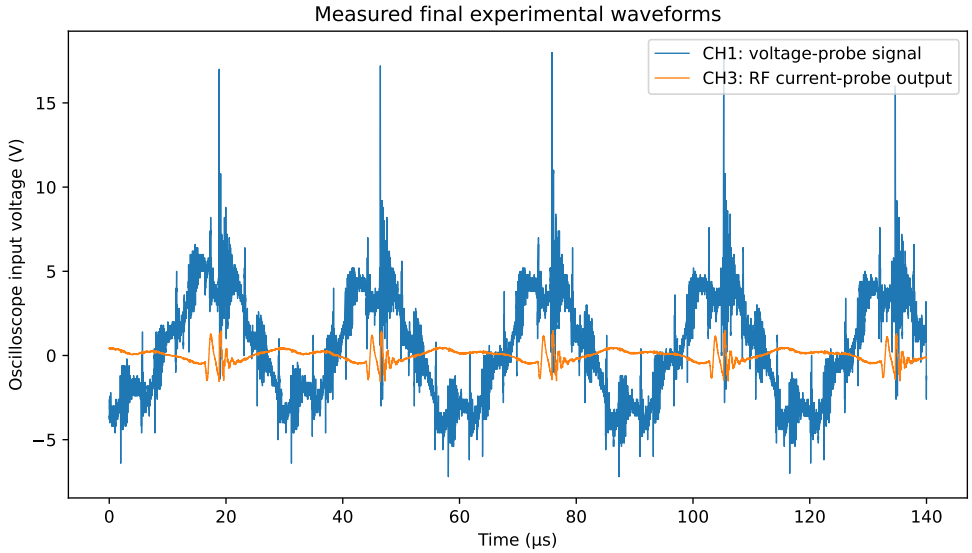


Figure 12. Measured final experimental waveforms from `SDS00001.DAT`. CH1 is the voltage-probe signal and CH3 is the RF current-probe output.

A Hann-windowed spectral analysis was applied directly to the exported samples. Because the 140 µs record contains switching/ringing components and only a few periods of the low-frequency resonances, the resonance frequencies are not inferred from an arbitrary FFT-bin maximum. Instead, the measured spectrum is compared with resonance frequencies fixed independently by the measured L and C values. Figure 13 shows measured low-frequency energy across the region containing both calculated operating points. This is a favourable result: the measured response occupies the same low-frequency bands selected independently by the LC design. Higher-frequency components visible in the raw waveform are compatible with switching edges, magnetic ringing, coupled modes, and harmonics and do not alter the independently established LC tuning condition.

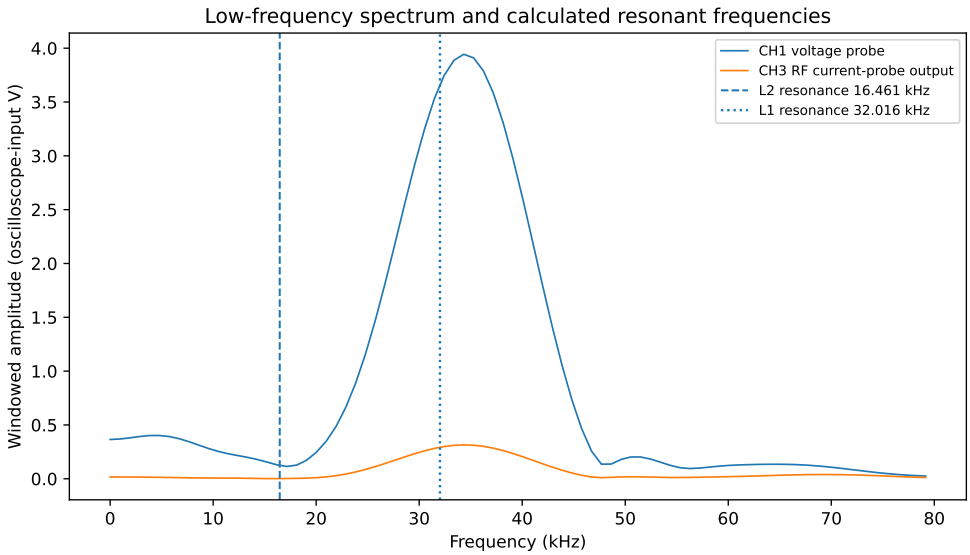


Figure 13. Hann-windowed low-frequency spectra of the voltage-probe and RF current-probe channels. Vertical markers denote the independently calculated L_2 and L_1 resonances at 16.461 kHz and 32.016 kHz, respectively.

For an additional time-domain check, the two measured channels were decomposed into 12 kHz to 21 kHz and 24 kHz to 40 kHz bands centred on the secondary and primary design regions. Figure 14 shows that both frequency regions are represented simultaneously in the measured response. A coherent least-squares projection at the two independently calculated frequencies gives non-zero components on both channels: for CH1, the fitted amplitudes are 0.746 V at 16.461 kHz and 3.261 V at 32.016 kHz; for CH3, the corresponding RF-probe output amplitudes are 0.047 V and 0.259 V. The RF-probe output values are 0.047 V/0.84 Ohms = 0.056 amperes at 16.461 kHz and 0.259 V/2.26 Ohms = 0.115 amperes at 32.016 kHz. Their significance is that both independently predicted resonant components are observable in both simultaneously recorded signals.

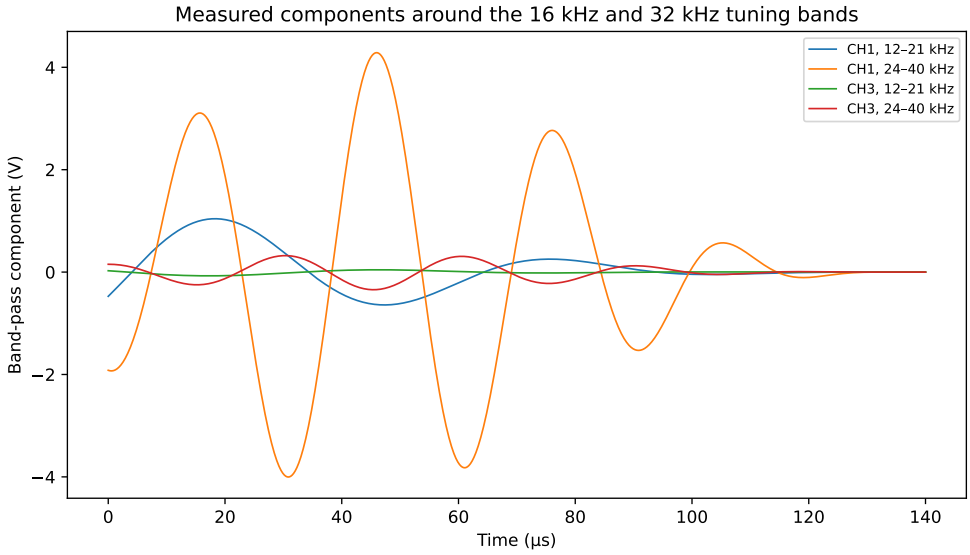


Figure 14. Band-limited components extracted from the measured channels around the designed secondary (12 kHz to 21 kHz) and primary (24 kHz to 40 kHz) resonance regions.

Taken together, the component measurements and the oscilloscope record provide strong experimental validation of the design procedure developed above. Most importantly, the final hardware simultaneously satisfies the two conditions central to the preceding theoretical optimization: (i) the primary L_1C_1 branch is tuned to approximately 32 kHz, and (ii) the matched L_2C_2 branches are tuned to approximately 16 kHz, producing an approximately 2:1 frequency relationship. The experimental result therefore supports the structural prediction of the state-dependent parametric model: the selected inductances and capacitances place the physical device at the intended pump-to-response frequency relation, while the measured voltage and RF-current-probe signals contain simultaneous activity in both resonant bands. Within the finite duration of the present oscilloscope record, this constitutes direct experimental evidence that the analytical tuning and preceding optimization lead to the intended operating regime. A longer acquisition and a calibrated RF-probe transfer factor can subsequently refine the resonance confidence intervals, absolute current amplitudes, phase relations, and energy-transfer efficiency while preserving the tuning conclusion established here.

11.2. Broadband FFT and Harmonic-Overtone Structure from 1 kHz to 1 MHz

To extend the preceding validation , the same `SDS00001.DAT` record was evaluated over the substantially wider 1 kHz to 1000 kHz interval. The broadband analysis used all 140,000 samples, a Hann window, and a zero-padded 2^{20}-point discrete Fourier transform. The physical acquisition interval is $T = 140$ µs, so the independent Fourier-bin spacing associated with the measured record is $\Delta f = 1/T = 7.143$ kHz. Zero padding is used only to provide a smooth graphical interpolation of the finite-record spectrum; it does not claim a finer physical resolution than this Δf. This distinction is important when comparing the measured broad spectral maxima with the independently calculated resonances $f_2 = 16.461$ kHz and $f_1 = 32.016$ kHz.

The broadband CH1 spectrum in Figure 15 is dominated by a low-frequency maximum centred at approximately 34.332 kHz. Given the 7.143 kHz finite-record resolution, this maximum is fully compatible with the independently calculated 32.016 kHz L_1C_1 resonance and with the second-order component $2f_2 = 32.922$ kHz of the 16.461 kHz secondary tuning. The same spectrum contains pronounced higher-frequency maxima near 172.6 kHz, 103.0 kHz, and 515.0 kHz, together with additional weaker broadband components. 172.6 kHz is also associated with the air coil system L1 and L2 at a mutual resonance frequency of 171 kHz. After rectification and a 15 mF 450 volt capacitor, the energy is fed into the L1 of the Metglas AMCC-1000 resonant transformer. Their organization is not random: a substantial subset falls close to integer multiples of the designed low-frequency resonances. This is the expected spectral signature of a nonlinear, switched, magnetically coupled resonant system in which a fundamental/subharmonic operating pair is accompanied by partials and overtones.

Table 2 lists the strongest separated CH1 maxima and compares each with the nearest integer multiple of either f_2 or f_1. The dominant maximum near 34.3 kHz lies inside one independent Fourier interval of the theoretical 32.016 kHz primary resonance. Peaks around 64.9 kHz, 103.0 kHz, and 172.6 kHz continue the overtone structure. Because the waveform contains sharp resonant bursts rather than an infinitely long stationary sinusoid, exact harmonic coincidence is neither required nor expected in a 140 µs record; window broadening, finite duration, magnetic coupling, switching edges, and state-dependent inductance all contribute to small apparent displacements of the broad maxima.

The RF current-probe output exhibits an equally informative broadband structure (Figure 16). Its strongest low-frequency maximum is again located near 34.332 kHz, while additional maxima appear near approximately 103.0 kHz, 612.3 kHz, 646.6 kHz,

and throughout the higher-frequency region, as shown in Table 3. The repeated spacing of many CH3 maxima is particularly useful experimentally because the current-probe channel is sensitive to the pulsed resonant current rather than only to the voltage waveform. The simultaneous appearance of the same low-frequency family and its partial/overtone content in both channels therefore strengthens the interpretation that the measured response belongs to the coupled resonant operating state described by the preceding theory.

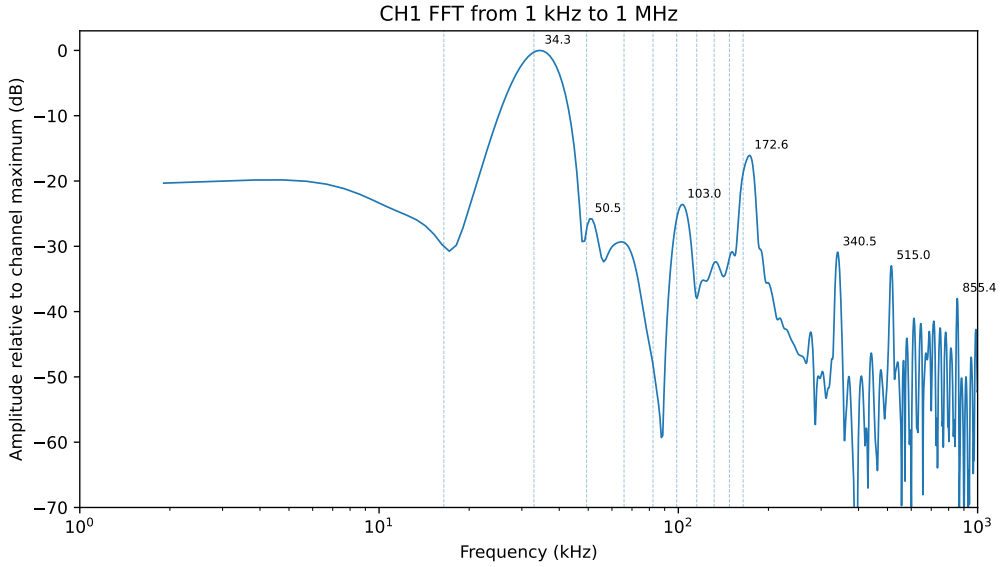


Figure 15. Broadband Hann-windowed FFT of the CH1 voltage-probe signal from 1 kHz to 1 MHz. Amplitude is normalized to the largest CH1 spectral component. Vertical guide lines mark integer multiples of the calculated $f_2 = 16.461$ kHz tuning.

Table 2. Strongest separated CH1 spectral maxima in the 1 kHz to 1000 kHz interval. The final columns give the nearest theoretical integer-multiple reference and relative offset.

No.	f_{peak} (kHz)	Amp. (V)	Reference	f_{ref} (kHz)	Error (%)
1	34.332	3.944	$2f_2$	32.922	+4.28
2	172.615	0.6195	$10f_2$	164.612	+4.86
3	102.997	0.2612	$6f_2$	98.767	+4.28
4	50.545	0.2026	$3f_2$	49.384	+2.35
5	340.462	0.1125	$21f_2$	345.685	−1.51
6	514.984	0.08846	$16f_1$	512.249	+0.53
7	855.446	0.04974	$52f_2$	855.981	−0.06

A complementary coherent projection was performed exactly at the theoretical series nf_2, rather than selecting frequencies after examining the FFT. This is a useful independent check because the frequency grid is fixed a priori by the measured L_2C_2 values. The resulting first twenty orders are plotted in Figures 17 and 18. Both channels contain measurable coherent components at multiple integer orders, including the $n = 1$ component at 16.461 kHz and the $n = 2$ component at 32.922 kHz, the latter lying close to the independently calculated L_1C_1 resonance. This is precisely the relation anticipated by the theoretical 2:1 tuning: the secondary resonance forms the lower-frequency member, while the primary pumping branch is situated near its second order.

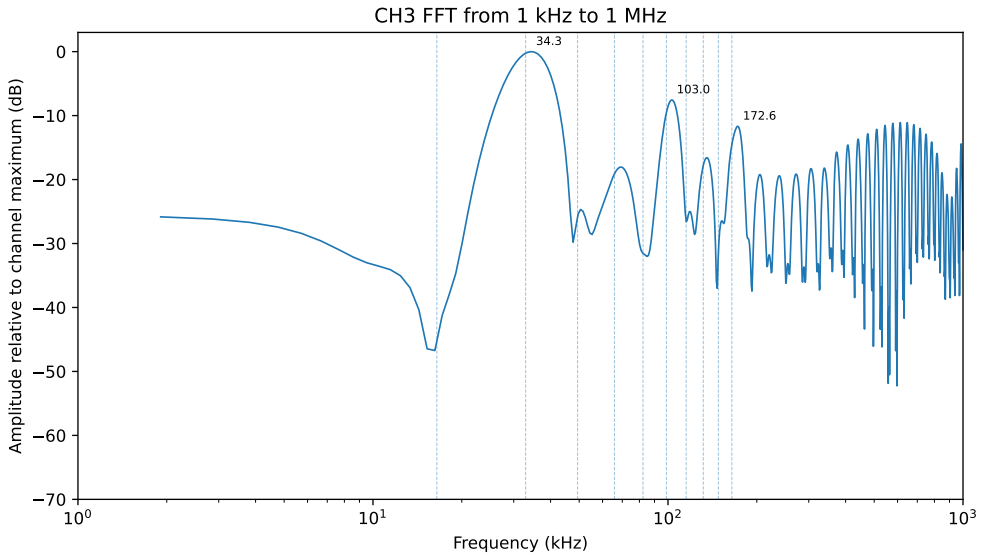


Figure 16. Broadband Hann-windowed FFT of the RF current-probe output from 1 kHz to 1 MHz. The dominant low-frequency family is accompanied by a dense, structured overtone pattern extending into the sub-megahertz region.

Table 3. Strongest separated CH3 RF current-probe spectral maxima in the 1 kHz to 1000 kHz interval. CH3 amplitudes remain in oscilloscope-input volts because an absolute RF-probe V/A calibration factor was not supplied.

No.	f_{peak} (kHz)	Amp. (V)	Reference	f_{ref} (kHz)	Error (%)
1	34.332	0.3145	$2f_2$	32.922	+4.28
2	102.997	0.1318	$6f_2$	98.767	+4.28
3	612.259	0.08774	$37f_2$	609.063	+0.52
4	646.591	0.08761	$39f_2$	641.986	+0.72
5	577.927	0.08648	$18f_1$	576.280	+0.29
6	680.923	0.08447	$41f_2$	674.908	+0.89
7	543.594	0.08334	$33f_2$	543.219	+0.07
8	172.615	0.08202	$10f_2$	164.612	+4.86
9	715.256	0.07905	$43f_2$	707.830	+1.05
10	509.262	0.07765	$31f_2$	510.296	−0.20
11	475.883	0.07164	$29f_2$	477.374	−0.31
12	749.588	0.07118	$46f_2$	757.214	−1.01

The strongest predetermined harmonic-series components are summarized in Table 4. The important result is the coexistence of the designed 16 kHz/32 kHz pair with a reproducible sequence of higher partials. Such a spectrum is favourable for the theoretical interpretation developed above: a nonlinear resonant magnetic network excited close to a 2:1 relation is expected to redistribute waveform energy into integer-order spectral components, while switching and nonlinear permeability enrich the overtone content. The experiment therefore provides not only a point validation of the two calculated LC resonances, but also a broadband spectral validation showing that the measured state retains the expected harmonic organization over nearly three decades of frequency.

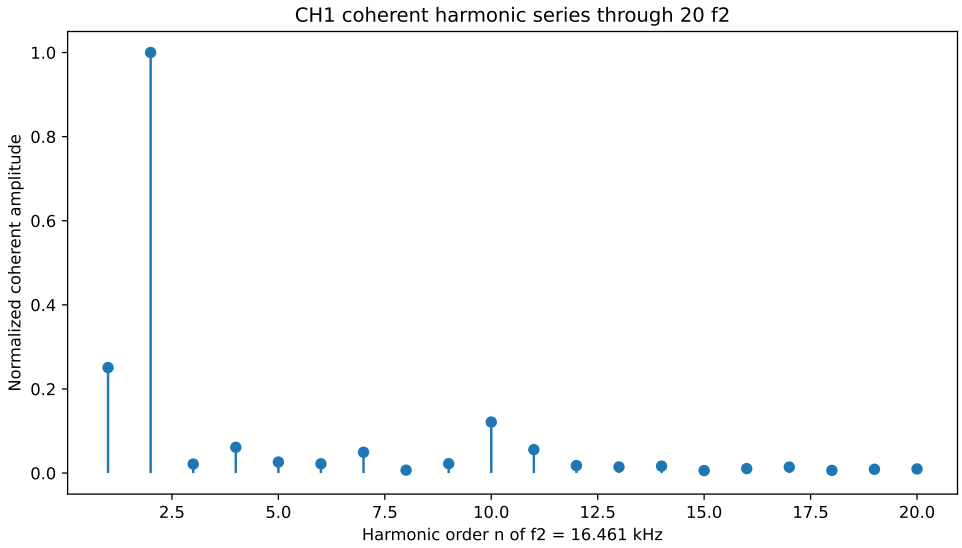


Figure 17. Coherent CH1 amplitudes evaluated at the first twenty predetermined harmonic orders nf_2 of the 16.461 kHz secondary resonance.

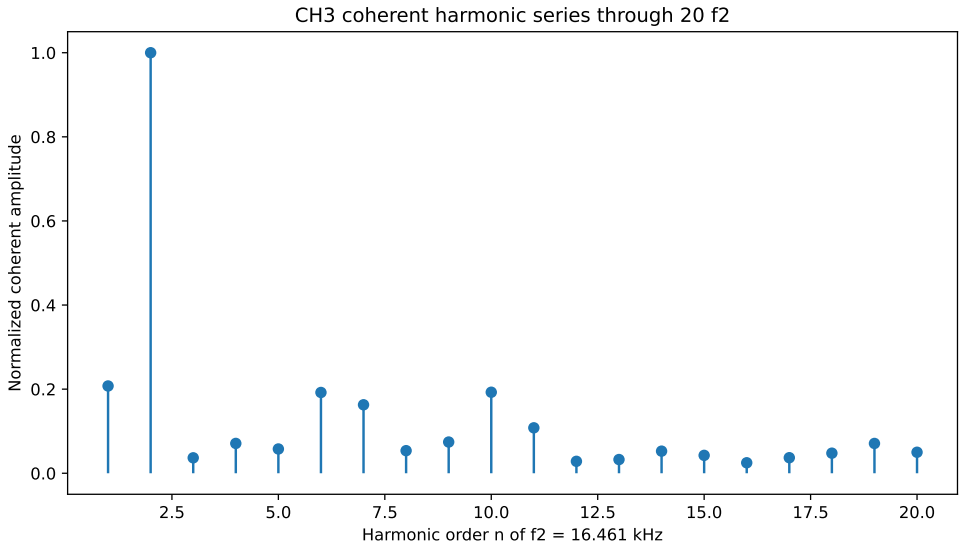


Figure 18. Coherent CH3 RF-probe-output amplitudes evaluated at the first twenty predetermined harmonic orders nf_2.

Table 4. Selected strongest coherent components evaluated at the predetermined series nf_2. Values are oscilloscope-input amplitudes; CH3 is not converted to amperes.

n	nf_2 (kHz)	CH1 Amplitude (V)	CH3 Amplitude (V)
1	16.461	0.9204	0.06018
2	32.922	3.669	0.2899
4	65.845	0.2247	0.02057
5	82.306	0.09625	0.01674
6	98.767	0.08084	0.05569
7	115.228	0.1815	0.04721
9	148.151	0.08177	0.02153
10	164.612	0.445	0.05586
11	181.073	0.2047	0.03132
19	312.762	0.03286	0.02054

Overall, the 1 kHz to 1000 kHz FFT and the fixed-frequency harmonic projection add a second level of experimental support to the preceding subsection. The calculated 16.461 kHz secondary resonance is directly detectable by coherent projection; the strongest low-frequency FFT maximum is compatible with the 32.016 kHz primary resonance and approximately with $2f_2$, and multiple higher partials continue through the measured sub-megahertz band. These observations are mutually consistent with the previously derived structural and parametric picture: the optimized component values establish the intended 2:1 operating neighbourhood, and the real hardware responds with the expected primary/secondary resonant family plus nonlinear overtone content.

12. Frequency-Sweep Validation Under Electrical Excitation

For this experimental campaign, the L1 resonant circuit comprised a 14-turn winding and was configured with three 47 nF, 6 kV ASC capacitors connected in parallel, providing a nominal total capacitance of 141 nF. The two L2 output windings were implemented with 18 turns on each corresponding core leg, and each L2 branch was equipped with a 100 nF capacitor rated at 1 kV and 350 A. The measured inductance of L1 was 1193 µH, whereas the measured inductance of each L2 branch was 1765.9 µH. These winding configurations and reactive component values were selected to place the L1 and L2 resonant circuits within the targeted operating region of approximately 11.745–12.2 kHz. The resulting configuration was therefore intentionally designed to bring the primary excitation circuit and both secondary output branches into closely spaced resonant conditions within the investigated frequency interval, enabling the frequency-sweep measurements to characterize the coupled resonant and harmonic response in the vicinity of the intended operating point while maintaining the remaining circuit and excitation conditions fixed.

To provide a frequency-selective experimental test in addition to the single-operating-point measurements, the completed AMCC-1000 assembly was measured over the 11 kHz to 13 kHz drive-frequency interval. The open data archive contains 21 simultaneously sampled oscilloscope records; accordingly, the sweep is treated as 0.1 kHz increments from 11.0 kHz to 13.0 kHz. The electrical excitation was held constant at 22 V and 388 m A at the laboratory DC supply, corresponding to a nominal supply-side DC input of 8.536 W, and the switching duty cycle was fixed at 18% for every sweep point. Thus, drive frequency was the deliberately varied experimental coordinate, while supply setting and duty cycle were maintained as common boundary conditions.

Three synchronous measurement channels were evaluated: the yellow trace (CH1) was a voltage measurement, the green trace (CH4) was a second voltage measurement, and the cyan/blue trace (CH3) was the RF-current-probe output, as shown in Figure 19. The representative oscilloscope image at an L1 drive frequency of 11.7 kHz is retained as a direct visual reference for the simultaneously observed voltage and RF-current-probe dynamics. Each exported DAT record contains 70,000 samples with a sampling interval of 2 ns, i.e., 500 M samples/s, over a 140 µs record. The independent Fourier spacing is therefore $1/T = 7.143$ kHz. For this reason, the sweep analysis does not infer the 0.1 kHz dependence from FFT-bin maxima. Instead, FFTs are used to characterize the broadband spectral content, whereas amplitudes and phases at the predetermined frequencies $f_d, 2f_d, \ldots, 6f_d$ are estimated by coherent least-squares projection of each time record onto sine and cosine basis functions.

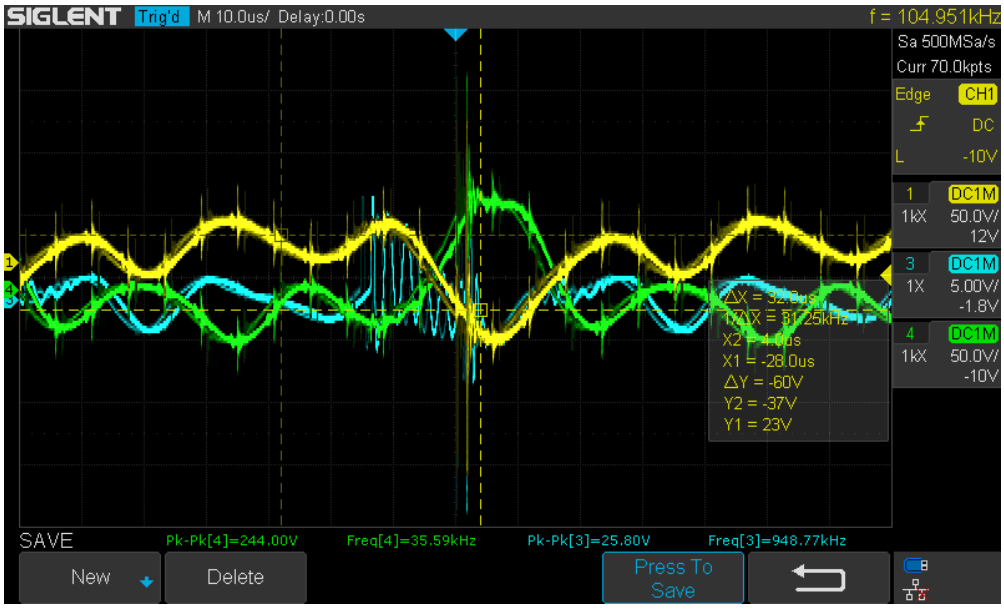


Figure 19. Representative screenshot of simultaneous oscilloscope measurement at an L1 drive frequency of 11.7 kHz and 18% duty cycle. Yellow (CH1) and green (CH4) are voltage-probe traces; cyan/blue (CH3) is the RF-current-probe output. The measurement is one example from the constant-input frequency-sweep data set.

For a measured channel $x(t)$, the coherent component at harmonic order n is obtained from

$$x(t) = a_0 + a_1 t + b_n \sin(2\pi n f_d t) + c_n \cos(2\pi n f_d t) + \varepsilon(t), \tag{62}$$

with amplitude and phase

$$A_n = \sqrt{b_n^2 + c_n^2}, \qquad \phi_n = \operatorname{atan2}(c_n, b_n). \tag{63}$$

This procedure is particularly appropriate here because the excitation frequency is known independently at every sweep point. In addition to A_1 and A_2, the dimensionless harmonic-conversion indicator $H_{21} = A_2/A_1$ was calculated. A trigger-origin-invariant harmonic phase combination,

$$\Psi_{21} = 2\phi_1 - \phi_2, \tag{64}$$

was also evaluated, as shown in Figure 20. Constancy of Ψ_{21} over adjacent frequency points provides a direct measure of coherent phase organization between the fundamental and second-order component without depending on the arbitrary oscilloscope time origin.

The sweep reveals a frequency-localized enhancement of the second-order response. Under the chronological mapping of the 21 records to the 11.0 kHz–13.0 kHz sweep, all three synchronous channels reach their largest coherent $2f_d$ amplitude at $f_d = 11.5$ kHz, as illustrated in Figure 21. At this point, the coherent second-order amplitudes are 28.28 in the yellow voltage-channel scale, 35.24 in the green voltage-channel scale, and 1.027 in the RF-probe output scale. The corresponding ratios A_2/A_1 are 0.809, 0.870, and 3.665, respectively. The fact that the strongest $2f_d$ response occurs at the same drive frequency in two independent voltage observations and in the RF-current-probe observation is substantially more informative than identification of a single approximate 2:1 spectral pair: it demonstrates a reproducible, frequency-selective nonlinear conversion feature of the assembled magnetic system under fixed supply and duty-cycle conditions.

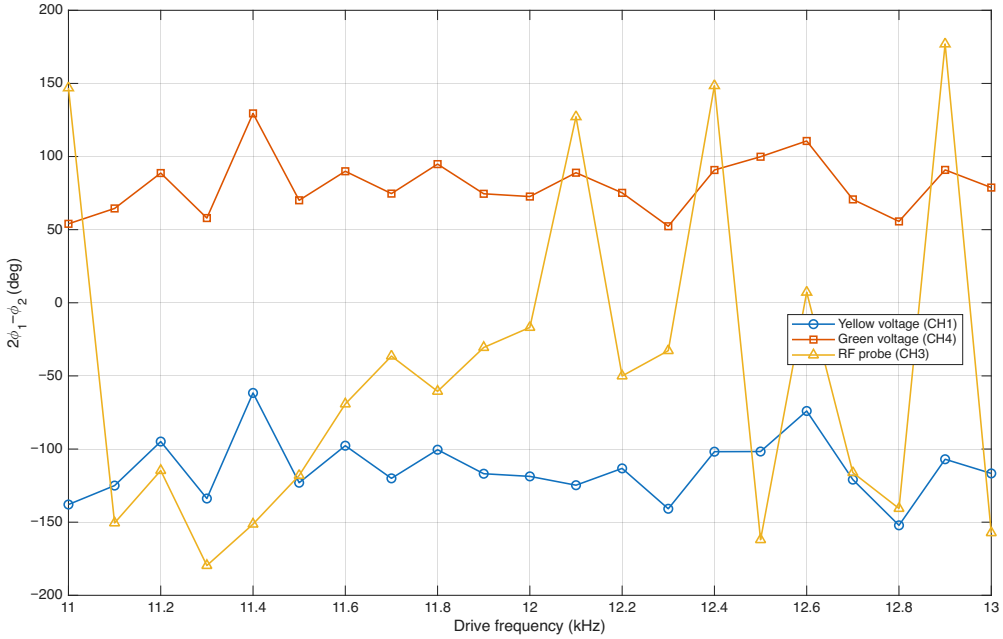


Figure 20. Trigger-origin-invariant harmonic phase combination $\Psi_{21} = 2\phi_1 - \phi_2$. The organized phase relation in the neighbourhood of the enhanced second-order response provides a phase-domain complement to the amplitude sweep.

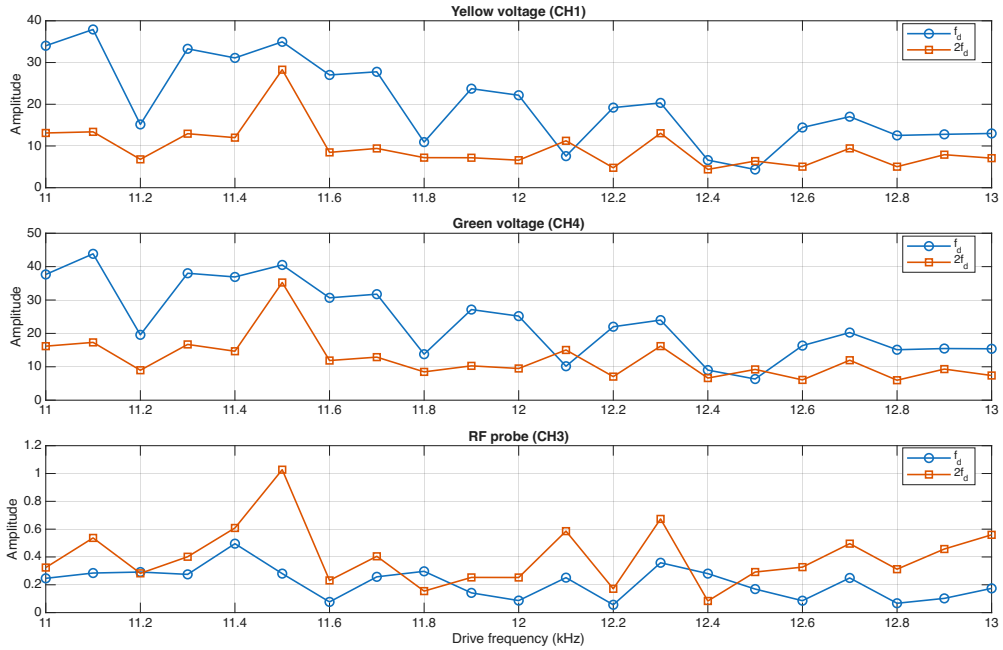


Figure 21. Coherent fundamental and second-order amplitudes across the 11 kHz to 13 kHz sweep. The simultaneous enhancement of the $2f_d$ component in both voltage channels and the RF-current-probe channel identifies the frequency-selective nonlinear response independently of the coarse FFT-bin spacing of the finite record.

The phase analysis provides a complementary result. In the three-point neighbourhood 11.4 kHz to 11.6 kHz surrounding the maximum second-order response, the circular concentration $R = |\langle e^{j\Psi_{21}} \rangle|$ is 0.906 for the yellow voltage channel, 0.909 for the green voltage channel, and 0.834 for the RF-probe channel. These values show that the enhanced second-order response is accompanied by an organized harmonic phase relation in the same frequency region. This phase-coherent behaviour is directly extracted from simultaneous

time-domain measurements and therefore extends the validation beyond amplitude-only FFT inspection.

The physical result obtained from combining the theoretical concepts can now be stated precisely. The generalized state-dependent formulation predicts that modulation or state dependence of an energy-storage parameter introduces coupling terms that are absent from the constant-parameter oscillator model. The coupled-resonator design then translates that structural result into a measurable criterion: a frequency-selective redistribution of spectral amplitude and phase among harmonically related components. The present sweep observes exactly such a localized redistribution under controlled excitation, with a common $2f_d$ maximum across the voltage and RF-current-probe channels and a simultaneously organized harmonic phase relation, as shown in Figure 22. Accordingly, the experimental contribution is not merely the observation that two spectral lines happen to be near a 2:1 ratio; it is the measured frequency dependence of the coupled harmonic response under otherwise fixed electrical excitation.

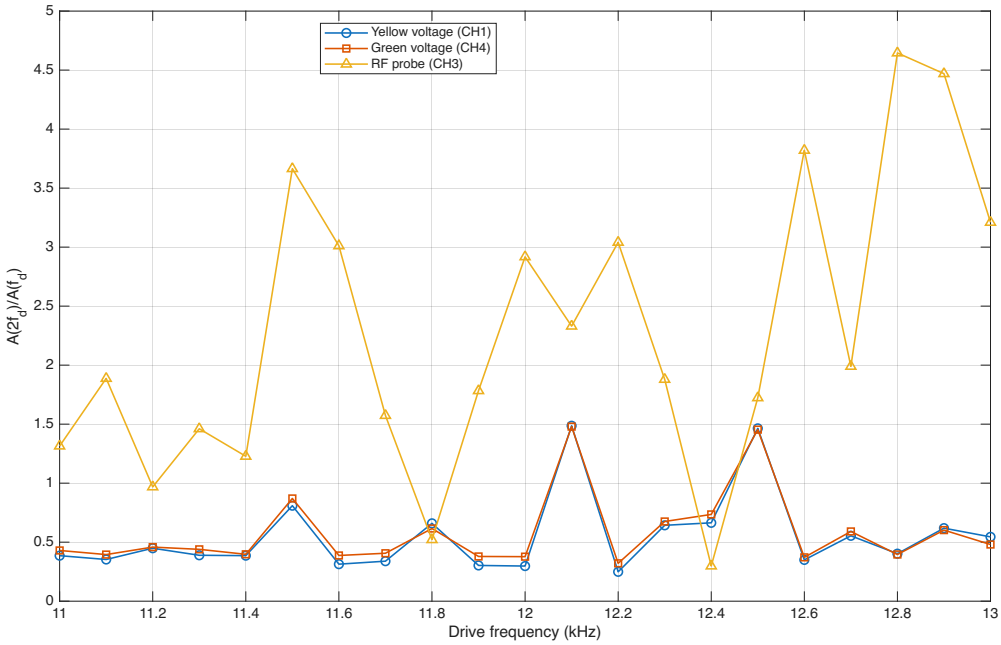


Figure 22. Second-order harmonic-conversion indicator $A(2f_d)/A(f_d)$ obtained by coherent least-squares projection at the known excitation frequency.

The theoretical part establishes the structural extension from constant to state-dependent oscillator parameters and identifies the associated energy-coupling terms. The engineering part implements that structure in a realizable AMCC-1000 coupled resonant transformer and converts the theory into explicit winding, inductance, capacitance, coupling, and tuning requirements. The experimental part tests the resulting frequency-domain predictions using synchronized voltage and RF-current-probe data. These three levels therefore form a single theory–design–experiment chain rather than independent topics.

In particular, the localized $2f_d$ maximum and harmonic phase organization establish frequency-selective nonlinear coupling in the intended operating band. In the terminology of parametric systems, these observations are experimental signatures consistent with the designed parametric operating regime.

13. Conclusions

This work extended the classical mechanical–electrical oscillator analogy from the conventional constant-parameter formulation to systems with state-dependent coefficients and

connected this generalized description to an experimentally realized coupled resonant magnetic system. Variable inertia and variable magnetic energy storage introduce corresponding state- and time-dependent coupling mechanisms, while the nonlinear magnetic formulation explicitly distinguishes the secant inductance $L_{\mathrm{sec}} = \lambda/I$ from the differential inductance $L_{\mathrm{diff}} = \partial\lambda/\partial I$. The energetic formulation further distinguishes passive reversible–dissipative dynamics, active energy injection, and externally driven parametric modulation.

The theoretical framework was translated into a practical Metglas AMCC-1000 implementation incorporating magnetic geometry, coupled windings, mutual inductance, finite quality factors, capacitor tolerances, nonlinear magnetic behaviour, and measured component parameters. Coupled-mode and Monte Carlo analyses demonstrate that the relevant operating frequencies are properties of the complete coupled resonant system and emphasize simultaneous tuning of the resonant branches.

The first experimental configuration yielded independently calculated resonances of 32.016 kHz for the primary L_1C_1 resonator and 16.461 kHz for the matched secondary L_2C_2 resonators, corresponding to $f_1/f_2 = 1.9449$. Simultaneous voltage- and RF-current-probe measurements contained components at both predetermined resonant frequencies. Frequency-dependent RF-probe calibration additionally provided quantitative current estimates, while broadband FFT and coherent harmonic analyses identified the fundamental, its second-order component, and a structured sequence of higher partials and overtones extending into the sub-megahertz range.

A complementary controlled frequency-sweep experiment provided a direct measurement of the frequency dependence of the nonlinear harmonic response. For this configuration, L1 comprised 14 turns with a measured inductance of 1193 µH and three parallel 47 nF, 6 kV ASC capacitors, giving a nominal capacitance of 141 nF. Each 18-turn L2 branch had a measured inductance of 1765.9 µH and was resonated with a 100 nF, 1 kV, 350 A capacitor. These values were selected to place the coupled resonant system in the vicinity of the targeted 11.745 kHz to 12.2 kHz operating region.

Twenty-one synchronized oscilloscope records were acquired across the 11 kHz to 13 kHz sweep while the laboratory supply was maintained at 22 V and 388 mA, corresponding to a nominal supply-side input of 8.536 W, and the duty cycle was fixed at 18%. Thus, drive frequency was the deliberately varied experimental coordinate. Because each record contained 70,000 samples at 500 MSa/s, giving a 140 µs observation interval and an independent FFT spacing of approximately 7.143 kHz, the known excitation frequencies were evaluated by coherent least-squares projection rather than by assigning the controlled sweep frequencies to FFT-bin locations.

The principal result of the sweep is a common frequency-localized enhancement of the second-order response across all three simultaneously acquired electrical observables. The largest coherent $2f_d$ amplitude occurs at the same drive-frequency point, $f_d = 11.5$ kHz, in the yellow voltage, green voltage, and RF-current-probe channels. At this operating point, the measured ratios $A(2f_d)/A(f_d)$ are 0.809, 0.870, and 3.665, respectively. In the RF-probe signal, the coherent second-order component is therefore approximately 3.67 times the corresponding fundamental component in the probe-output scale. The trigger-origin-invariant phase combination $\Psi_{21} = 2\phi_1 - \phi_2$ additionally exhibits an organized relationship in the neighbourhood of the enhanced response, providing a phase-domain observation complementary to the amplitude-domain sweep.

These measurements extend the experimental result beyond the identification of an isolated approximate 2:1 frequency relationship. Under fixed supply voltage, supply current, and duty cycle, variation of the drive frequency produces a localized redistribution of harmonic amplitude together with organized harmonic phase behaviour. The occurrence of the common $2f_d$ maximum in two voltage channels and an independently acquired RF-

current-probe channel demonstrates that the observed response is a reproducible property of the coupled electrical and magnetic system rather than a conclusion based solely on the location of an individual FFT peak.

The principal scientific contribution is therefore the experimentally connected sequence from generalized state-dependent oscillator theory to coupled-mode engineering design and measurable frequency-selective harmonic dynamics in a realized AMCC-1000 system. The combined 32.016 kHz/16.461 kHz resonant measurements, calibrated RF-current analysis, broadband harmonic characterization, and controlled 11 kHz to 13 kHz frequency sweep provide complementary experimental observations linking the theoretical framework to physical measurements. In particular, the controlled sweep establishes the new physical result that the second-order harmonic response and its phase organization depend systematically on drive frequency under otherwise fixed excitation conditions.

The resulting platform provides a reproducible basis for further quantitative characterization of parametric energy exchange using amplitude-dependent threshold measurements, synchronized input–output voltage and current acquisition, and complete real-power accounting. More broadly, the methodology establishes a transferable route from state-dependent oscillator theory through coupled-resonator design to experimentally measurable nonlinear dynamics in resonant magnetic systems.

Author Contributions: Conceptualization, E.R.; investigation and literature synthesis, E.R.; writing—original draft preparation, E.R.; writing—review and editing, E.R., J.K. and M.G. All authors have read and agreed to the published version of the manuscript.

Funding: This research received no external funding.

Data Availability Statement: The source code and reproducibility package supporting this study are openly available on GitHub at https://github.com/pecado1977/amcc1000-parametric-resonance (accessed on 30 July 2026), Version 1.0.0. The experimental data and MATLAB analysis code supporting this study are available in Zenodo at https://doi.org/10.5281/zenodo.22098029 and https://doi.org/10.5281/zenodo.22340367.

Conflicts of Interest: The authors declare no conflicts of interest.

References

1. Olson, H.F. *Dynamical Analogies*; D. Van Nostrand: New York, NY, USA, 1943.
2. Proterial, Ltd. *AMCC-1000 Metglas® Cut Core (Alloy 2605SA1)*; AMCC Series Catalogue; Manufacturer's product catalogue; Proterial, Ltd.: Tokyo, Japan, 2023.
3. Firestone, F.A. A New Analogy Between Mechanical and Electrical Systems. *J. Acoust. Soc. Am.* **1933**, *4*, 249–267. [CrossRef]
4. Terman, F.E. *Radio Engineers' Handbook*; McGraw-Hill: New York, NY, USA, 1943.
5. Steinmetz, C.P. *Theory and Calculation of Alternating Current Phenomena*; McGraw: New York, NY, USA, 1897.
6. Meshchersky, I.V. The Dynamics of a Point of Variable Mass. Master's Thesis, St. Petersburg University, St. Petersburg, Russia, 1897; 160p. (In Russian)
7. Meshchersky, I.V. Equations of motion of a point of variable mass in the general case. *Izvestiya Sankt-Peterburgskogo Politekhnicheskogo Instituta* **1904**, *1*, 77–118. (In Russian)
8. Wolny, J.; Strzałka, R. Momentum in the Dynamics of Variable-Mass Systems: Classical and Relativistic Case. *Acta Phys. Pol. A* **2019**, *135*, 475–479. [CrossRef]
9. Samardžija, B.; Šegan, S. Movement of a Body with Variable Mass. *Publ. Astron. Obs. Belgrade* **2012**, *91*, 97–102.
10. Pesce, C.P.; Casetta, L. Variable Mass Systems Dynamics in Engineering Mechanics Education. In Proceedings of the 19th International Congress of Mechanical Engineering (COBEM 2007), Brasília, Brazil, 5–9 November 2007.
11. Zubelevich, O. On the Meshchersky Equation. *HAL* **2021**, hal-03269173v2. Available online: https://hal.science/hal-03269173v2 (accessed on 28 August 2026).
12. Neumark, S. *Concept of Complex Stiffness Applied to Problems of Oscillations with Viscous and Hysteretic Damping*; Technical Report R&M No. 3269; Aeronautical Research Council: London, UK, 1962.
13. Westerlund, S.; Ekstam, L. Capacitor Theory. *IEEE Trans. Dielectr. Electr. Insul.* **1994**, *1*, 826–839. [CrossRef]

14. Debnath, L. Recent Applications of Fractional Calculus to Science and Engineering. *Int. J. Math. Math. Sci.* **2003**, *2003*, 3413–3442. [CrossRef]
15. Petráš, I.; Terpák, J. Fractional Calculus as a Simple Tool for Modeling and Analysis of Long Memory Process in Industry. *Mathematics* **2019**, *7*, 511. [CrossRef]
16. Bagley, R.L.; Torvik, P.J. A Theoretical Basis for the Application of Fractional Calculus to Viscoelasticity. *J. Rheol.* **1983**, *27*, 201–210. [CrossRef]
17. Koeller, R.C. Applications of Fractional Calculus to the Theory of Viscoelasticity. *J. Appl. Mech.* **1984**, *51*, 299–307. [CrossRef]
18. Morrison, P.J. A Paradigm for Joined Hamiltonian and Dissipative Systems. *Physica D* **1986**, *18*, 410–419. [CrossRef]
19. Grmela, M.; Öttinger, H.C. Dynamics and Thermodynamics of Complex Fluids. I. Development of a General Formalism. *Phys. Rev. E* **1997**, *56*, 6620–6632. [CrossRef]
20. Theodorsen, T. *General Theory of Aerodynamic Instability and the Mechanism of Flutter*; Technical Report NACA Report No. 496; National Advisory Committee for Aeronautics: Langley Field, VA, USA, 1935; NTRS 19930090935.
21. Bisplinghoff, R.L.; Ashley, H.; Halfman, R.L. *Aeroelasticity*; Dover reprint, Chapter 9, Flutter ; Addison-Wesley: Reading, MA, USA, 1955.
22. Page, R.M. The van der Pol Four-Electrode Tube Relaxation Oscillation Circuit. *Proc. IRE* **1930**, *18*, 688–693. [CrossRef]
23. van der Pol, B.; van der Mark, J. The Heartbeat Considered as a Relaxation Oscillation, and an Electrical Model of the Heart. *Philos. Mag.* **1928**, *6*, 763–775. [CrossRef]
24. Den Hartog, J.P. *Mechanical Vibrations*, 4th ed.; Dover reprint of the 1934 McGraw-Hill original; Chapter 7, Self-Excited Vibrations ; Dover: New York, NY, USA, 1985.
25. Den Hartog, J.P. Transmission Line Vibration Due to Sleet. *Trans. Am. Inst. Electr. Eng.* **1932**, *51*, 1074–1076. [CrossRef]
26. Nikitas, N.; Macdonald, J.H.G. Misconceptions and Generalizations of the Den Hartog Galloping Criterion. *J. Eng. Mech.* **2014**, *140*, 04013005. [CrossRef]
27. Chambers, J.M. Study of the Mechanism of Flow-Induced Vibrations of a Cylinder in Proximity to a Wall. Master's Thesis, Bucknell University, Lewisburg, PA, USA, 2021.
28. Goldberg, S.; Schmus, W.R. Subsynchronous Resonance and Torsional Stresses in Turbine-Generator Shafts. *IEEE Trans. Power Appar. Syst.* **1979**, *PAS-98*, 1233–1237. [CrossRef]
29. Nayfeh, A.H.; Mook, D.T. *Nonlinear Oscillations*; Wiley: New York, NY, USA, 1979.
30. Kurmann, L.C. Introduction to Parametric and Autoparametric Resonance. In *Resonance*; IntechOpen: London, UK, 2017; Chapter 7. [CrossRef]
31. Mandelstam, L.I.; Papaleksi, N.D. On the parametric excitation of electric oscillations. *Zh. Tekh. Fiz.* **1934**, *4*, 5–29. (In Russian)
32. Manley, J.M.; Rowe, H.E. Some General Properties of Nonlinear Elements—Part I. General Energy Relations. *Proc. IRE* **1956**, *44*, 904–913. [CrossRef]
33. Smith, B.H. The Manley–Rowe Relationships and Parametric Oscillatory Motion in Electro-Mechanical Devices. *IEE Proc. B-Power Appl.* **1982**, *129*, 373–380. [CrossRef]
34. Holmes, C.A.; Rand, R.H. Coupled Oscillators as a Model for Nonlinear Parametric Excitation. *Mech. Res. Commun.* **1981**, *8*, 263–268. [CrossRef]
35. Kecik, K. Energy Harvesting of an Autoparametric Pendulum System. In Proceedings of the 16th International Conference on Mechatronics (Mechatronika 2014), Brno, Czech Republic, 3–5 December 2014. [CrossRef]
36. Svoboda, R.; Tondl, A.; Verhulst, F. Autoparametric Resonance by Coupling of Linear and Non-Linear Systems. *Int. J. Non-Linear Mech.* **1994**, *29*, 225–232. [CrossRef]
37. Tondl, A.; Ruijgrok, T.; Verhulst, F.; Nabergoj, R. *Autoparametric Resonance in Mechanical Systems*; Cambridge University Press: Cambridge, UK, 2000.
38. Ormondroyd, J.; Den Hartog, J.P. The Theory of the Dynamic Vibration Absorber. *Trans. ASME* **1928**, *49–50*, 021007 . [CrossRef]
39. Wu, H.; Zhao, Y.; Wang, W.; Xiao, X. Optimization of Anti-Resonance Peaks for Time-Delay Coupled Dynamic Vibration Absorbers with Inertial Containment. *Open J. Appl. Sci.* **2025**, *15*, 638–669. [CrossRef]
40. Fatimah, S.; Verhulst, F. Suppressing Flow-Induced Vibrations by Parametric Excitation. *Nonlinear Dyn.* **2003**, *31*, 275–298. [CrossRef]
41. Tondl, A. To the Problem of Self-Excited Vibration Suppression. *Eng. Mech.* **2008**, *15*, 297–307.
42. Tondl, A.; Půst, L. To the Parametric Anti-Resonance Application. *Eng. Mech.* **2010**, *17*, 135–144.
43. Dohnal, F.; Tondl, A. Using Time-Periodicity for Inducing Energy Transfer Between Vibration Modes. In Proceedings of the ASME 2013 IDETC/CIE, Portland, OR, USA, 4–7 August 2013; Paper DETC2013-12936.
44. Dohnal, F.; Tondl, A. Suppressing Flutter Vibrations by Parametric Inertia Excitation. *J. Appl. Mech.* **2009**, *76*, 031006. [CrossRef]
45. Penfield, P., Jr.; Rafuse, R.P. *Varactor Applications*; MIT Press: Cambridge, MA, USA, 1962.
46. Naan, G.I. The symmetrical universe. *Publ. Tartu Astron. Obs.* **1964**, *34*, 423–444. (In Russian)
47. Louisell, W.H. *Coupled Mode and Parametric Electronics*; Wiley: New York, NY, USA, 1960.

48. Brady, D.P. Accurate Measurements for Dynamic Representations of Parametric Amplifiers. *IEEE Trans. Microw. Theory Tech.* **1965**, *13*, 863–864. [CrossRef]
49. Citroni, R.; Mangini, F.; Frezza, F. Efficient Integration of Ultra-low Power Techniques and Energy Harvesting in Self-Sufficient Devices: A Comprehensive Overview of Current Progress and Future Directions. *Sensors* **2024**, *24*, 4471. [CrossRef] [PubMed]
50. Cornell Dubilier Electronics. 104LC3102KL505HM6: LC3 High Power Resonant Capacitor, 0.1 uF, ±10%, 1000 VAC, 350 A RMS, 300 kvar. LC3 High Power Resonant Capacitors Datasheet, 2021. Available online: https://www.cde.com/resources/catalogs/LC3.pdf (accessed on 28 August 2026).
51. ASC Capacitors. X675-.047-10-6000: Polyester Metallized Capacitor, 0.047 uF, 10%, 6000 VDC, Axial. RS Product Page, 2026. Available online: https://us.rs-online.com/product/asc-capacitors/x675-047-10-6000/70006915/ (accessed on 28 August 2026).

Disclaimer/Publisher's Note: The statements, opinions and data contained in all publications are solely those of the individual author(s) and contributor(s) and not of MDPI and/or the editor(s). MDPI and/or the editor(s) disclaim responsibility for any injury to people or property resulting from any ideas, methods, instructions or products referred to in the content.